Electron Scattering via Geometric and Dynamical Decoupling

Lorenzo Bagnasacco, 1, * Fabio Taddei, 1 and Vittorio Giovannetti 1

¹NEST, Scuola Normale Superiore and Istituto Nanoscienze-CNR, Piazza dei Cavalieri 7, I-56126 Pisa, Italy

By decoupling the geometric from the dynamical contributions in the scattering dynamics, we develop a method to compute the scattering matrix of electrons in a one-dimensional coherent conductor connected to two electrodes. In particular, we demonstrate that, in the high-energy regime, the transmission matrix converges to the Berry operator of the system. We showcase the method through several examples featuring different in-plane magnetic field profiles. Notably, our results reveal the possibility of achieving near-perfect spin-flip transmission, highlighting potential applications in spintronics.

I. INTRODUCTION

Understanding the scattering properties of electrons in mesoscopic systems is essential for advancing spin-dependent transport technologies [1–3]. Such properties are encoded in the elements of a matrix known as the scattering matrix [4–6]. In quantum transport theory [7–9], specifically in the context of mesoscopic physics and nanostructures, the scattering matrix is a fundamental object that describes how incoming quantum states are transformed into outgoing states as a result of scattering processes within a conductor or device.

In this work, we present a novel method—building on Ref. [10]—for computing the spin-resolved scattering matrix of a coherent conductor, within the well-known Landauer-Büttiker formalism [11]. The key innovation lies in separating the geometric Berry operator [12] of the system from the dynamical evolution in the scattering dynamics. Differently from Ref. [10], which assumes the particle energy to be infinite, our method is exact and applicable to arbitrary energies.

As a concrete setup, we consider a 1D wire and calculate the scattering amplitudes which describe the spin-dependent transport in the presence of a spatially varying Zeeman field, see Fig. 1. This is a typical situation addressed in *spintronics*, the research field which concerns the investigation of spin-dependent transport [13–15] and its applications (see the review papers in Refs. [16–19]). In particular, we demonstrate that the transmission and reflection matrices of the setup can be calculated by solving a differential equation which contains both geometric and dynamical contributions.

To better elucidate these facts we consider two different examples where the vector representing the spatially varying magnetic field lies in a plane. In the first one, the magnetic field in the leads points in opposite directions (see panel a) of Fig. 1), while in the second it points in orthogonal directions (see panel b) of Fig. 1). In both cases we consider different profiles of variation of magnetic fields characterized by two parameters we plot the spin-dependent transmission and probabilities as functions of energy E of the impinging electron.

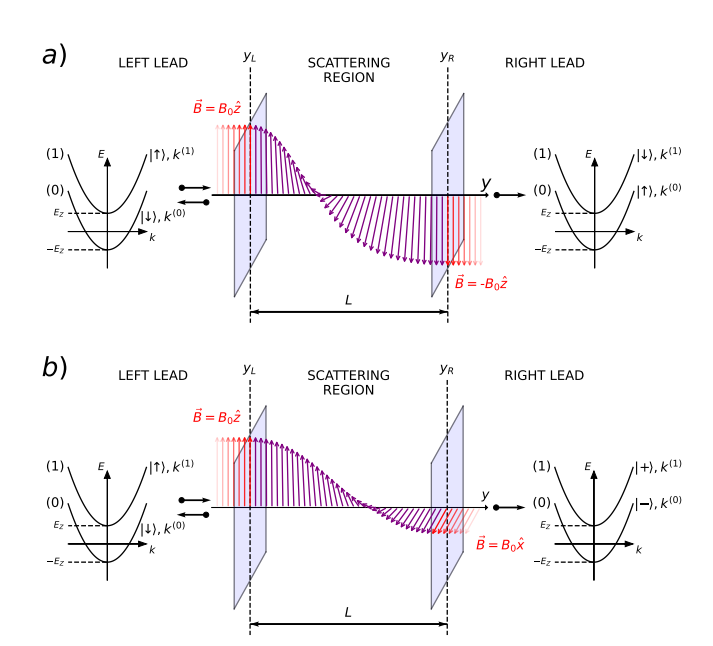


FIG. 1. Schematic of the model: electrons propagates on a 1D wire parametrized by the longitudinal coordinate y, under the action of an external, static magnetic field. The wire is composed by three distinct regions: the left lead $(y < y_L)$, the right lead $(y_R < y)$ where the magnetic field is uniform, assuming constant values $B_{\rm L}$ and $B_{\rm R}$, respectively, and the scattering region $(y_L < y < y_R)$ where instead the magnetic field vector B(y) (represented by purple vectors) can vary. Panel a): The plot shows the y-varying magnetic field B(y)of the scheme I of Sec. VIA, with components given in (62) setting $q_1 = 0$ and $q_2 = 0$. In this specific case, the magnetic field has only a positive z component in the left lead and a negative z components in the right lead. Panel b): The plot shows the y-varying magnetic field B(y) of the scheme II of Sec. VIB, with components given by Eq. (68) setting $q_1 = 0$ and $q_2 = 0$. In this case, the magnetic field has only a positive z component in the left lead and a negative x components in the right lead. To enhance clarity, we have aligned the directions n_1 and n_3 , which define the magnetic field orientation along the wire as described in Eq. (58), with the x- and z-axis, respectively. Dispersion curves for the leads are shown on the sides of the plots.

We first show that it is possible to find profiles such that, for E below the Zeeman splitting energy in the leads, nearly perfect spin-flip transmission can be ob-

^{*} lorenzo.bagnasacco@sns.it

tained (first example), while an electron in the spin-down spin state can be perfectly transmitted in a balanced superposition of the spin-down and spin-up spin states (second example). Moreover, we find that the transmission probabilities strongly depend on the particular magnetic field profile (through the two parameters), and when E is by far the largest energy scale in the system, we find that the transmission matrix coincides with the Berry operator as predicted. In particular, in the first example we find that while the spin state of the transmitted electron remains the same, its wave vector changes, while, in the second example, we show that the transmitted electron is in an entangled state between the spin and momentum degree of freedom. To conclude, we highlight a notable result: in the limiting case of infinite energy the transmission matrix coincides with the Berry operator of the system.

The paper is organized as follows: in Sec. II we introduce the model and present some preliminary remarks; in Sec. III the scattering problem is solved by decoupling the geometric contribution from the rest; Sec. IV focuses on special cases that allow for a fully analytical treatment i.e. the infinite energy limit (Sec. IV A), the infinitesimal scattering region limit (Sec. IV B), and the piecewise constant regime (Sec. IV C); Sec. V is dedicated to compute explicitly the Berry operator for control induced by varying a Zeeman field; in Sec. VI numerical examples are presented to illustrate the results. The conclusions are summarized in Sec. VII, and a series of appendices provide detailed technical derivations of the main results.

II. PHYSICAL MODEL

The Hamiltonian describing the propagation of electrons in a 1D wire under the action of a position-dependent magnetic field B(y) writes

$$\hat{\mathcal{H}} := \frac{\hat{p}_y^2}{2m} - \boldsymbol{\mu}_s \cdot \boldsymbol{B}(y) , \qquad (1)$$

with $p_y := -(i/\hbar)\partial_y$ denoting the electron momentum operator \hat{p}_y along the longitudinal axis y of the device and μ_s the electronic spin magnetic momentum. Indicating with g(>0) the Landé factor, $\mu_B(>0)$ the Bohr magneton, and $\hat{\boldsymbol{\sigma}} := (\hat{\sigma}_x, \hat{\sigma}_y, \hat{\sigma}_z)$ the vector of Pauli operators, the second contribution of $\hat{\mathcal{H}}$ can be expressed

$$\hat{h}_y := -\boldsymbol{\mu}_s \cdot \boldsymbol{B}(y) = g\mu_B B(y) \hat{\sigma}_{\boldsymbol{n}(y)} , \qquad (2)$$

where $B(y) := |\mathbf{B}(y)|$ and $\mathbf{n}(y) := \mathbf{B}(y)/B(y)$ indicate respectively the magnitude and the orientation of the magnetic field at position y, and $\hat{\sigma}_{\mathbf{n}(y)} := \mathbf{n}(y) \cdot \hat{\boldsymbol{\sigma}}$ is the spin operator component along $\mathbf{n}(y)$. For fixed y, the

eigenvectors of \hat{h}_{y} identify the Zeeman spin-eigenstates,

$$\hat{h}_{y} |\phi_{\boldsymbol{n}_{y}}^{(\ell)}\rangle = E_{\mathbf{Z}_{y}}^{(\ell)} |\phi_{\boldsymbol{n}_{y}}^{(\ell)}\rangle, \quad E_{\mathbf{Z}_{y}}^{(\ell)} := -(-1)^{\ell} g\mu_{B} |\boldsymbol{B}(y)|,$$
(3)

with $\ell = \{0, 1\}$. In particular, we will refer to $|\phi_{\boldsymbol{n}(y)}^{(0)}\rangle$ as the (local) lower-energy Zeeman spin-eigenstate, while to $|\phi_{\boldsymbol{n}(y)}^{(1)}\rangle$ as the (local) higher-energy Zeeman spin-eigenstate (recall that $g\mu_B$ is positive).

In our analysis, we partition the wire into three distinct regions: the left lead $(y \leq y_L)$, the right lead $(y_R \leq y)$, and the scattering region $(y_L < y < y_R)$, see Fig. 1. In the left and right leads, the magnetic field is uniform, assuming constant values $B_{\mathrm{L}} := |B_{\mathrm{L}}| n_{\mathrm{L}}$ and $\boldsymbol{B}_{\mathrm{R}} := |\boldsymbol{B}_{\mathrm{R}}| \boldsymbol{n}_{\mathrm{R}},$ respectively. We assume the magnitudes of these fields are equal, such that $|B_L| = |B_R| = B_0$ while allowing their orientations, denoted as $n_{\rm L}$ and $n_{\rm R}$, to differ. In contrast, the magnetic field in the scattering region is not constant providing a somehow smooth transition between $B_{\rm L}$ and $B_{\rm R}$ (more precisely we shall require B(y) be differentiable everywhere with first derivative that is continuous at the interface between the leads and the scattering region). In virtue of these assumptions in the leads the system exhibits spin-resolved energy bands

$$E^{(\ell)}(k) := \frac{\hbar^2 k^2}{2m} + E_{\mathbf{Z}}^{(\ell)} \qquad \ell \in \{0, 1\} , \qquad (4)$$

where $E_{\mathbf{Z}}^{(\ell)} := -(-1)^{\ell} g \mu_B B_0$ are the eigenvalues (3) evaluated outside the scattering region, whose gap

$$E_{\rm Z} := \frac{E_{\rm Z}^{(1)} - E_{\rm Z}^{(0)}}{2} = g\mu_B B_0 , \qquad (5)$$

defines the fundamental energy scale of the problem. Electrons with sufficiently high energy E can occupy these bands. Their redistribution across the scattering region, as well as the current flowing through the device, is governed by the transmission and reflection scattering matrices t_E and r_E of the model. Computing them accounts in solving the energy-resolved Schrödinger equation of the setup, i.e.

$$(\hat{\mathcal{H}} - E) |\psi_y^{(E)}\rangle = -\frac{\hbar^2}{2m} \partial_y^2 |\psi_y^{(E)}\rangle + (\hat{h}_y - E) |\psi_y^{(E)}\rangle = 0 ,$$
(6)

with $|\psi_y^{(E)}\rangle$ the spinor wave-function associated with energy eigenvalue E. In the leads the solution of Eq. (6) can be expressed as

$$|\psi_{y}^{(E)}\rangle = \begin{cases} \sum_{\ell \in \{0,1\}} \left(A_{E}^{(\ell)} e^{ik_{E}^{(\ell)} y} + R_{E}^{(\ell)} e^{-ik_{E}^{(\ell)} y} \right) |\phi_{\mathbf{n}_{L}}^{(\ell)}\rangle, \\ \forall y \leq y_{L} \\ \sum_{\ell \in \{0,1\}} T_{E}^{(\ell)} e^{ik_{E}^{(\ell)} y} |\phi_{\mathbf{n}_{R}}^{(\ell)}\rangle, \quad \forall y \geq y_{R}, \end{cases}$$

$$(7)$$

with $|\phi_{n_{\rm L/R}}^{(\ell)}\rangle$ the Zeeman eigenvectors (3) evaluated for

 $y = y_{\rm L}, y_{\rm R}$ respectively, and

$$k_E^{(\ell)} := \sqrt{2m(E - E_Z^{(\ell)})}/\hbar ,$$
 (8)

determined by the dispersion relation (4) by imposing the constraint $E^{(\ell)}(k) = E$. We emphasize that for $E \leq E_{\mathbf{Z}}^{(\ell)}$ the coefficients $A_E^{(\ell)}$, $R_E^{(\ell)}$ and $T_E^{(\ell)}$ describe evanescent waves. These waves decay exponentially with distance from the scattering region and, as a result, do not carry any current. In contrast for $E > E_{\rm Z}{}^{(\ell)}, \ A_E^{(\ell)}, R_E^{(\ell)}$, and $T_E^{(\ell)}$ characterize the asymptotic behaviour of $|\psi_y^{(E)}\rangle$ far away from the scattering region. Specifically in this regime $A_E^{(\ell)}$ represents right-going electrons injected into the ℓ -th energy band (4) of the left lead, $R_E^{(\ell)}$ denotes the associated amplitude of left-going reflected electrons, and $T_E^{(\ell)}$ the amplitude of right-going transmitted electrons. The functional dependence among these terms, determined by explicitly solving Eq. (6), define the transmission t_E and reflection r_E matrix of the model.

Consider for instance the two-channel regime where Eexceeds the biggest Zeeman eigenvalues in the leads, i.e.

$$E > E_{\rm Z}^{(1)} = E_{\rm Z} \ .$$
 (9)

In this regime, both the energy bands of the system can be populated, and t_E and r_E correspond to 2×2 matrices. The elements of these matrices are defined by the following relations:

$$[t_E]_{\ell,\ell'} := \tau_E^{(\ell,\ell')} \sqrt{\frac{k_E^{(\ell)}}{k_E^{(\ell')}}}, \quad [r_E]_{\ell,\ell'} := \rho_E^{(\ell,\ell')} \sqrt{\frac{k_E^{(\ell)}}{k_E^{(\ell')}}}, \quad (10)$$

where $\tau_E^{(\ell,\ell')}$ and $\rho_E^{(\ell,\ell')}$) are, respectively, the values of amplitudes $T_E^{(\ell)}$ and $R_E^{(\ell)}$ appearing in Eq. (7) that emerge when we take $A_E^{(\ell)} = \delta_{\ell,\ell'}$. In particular, $[t_E]_{\ell,0}$ (resp. $[r_E]_{\ell,0}$) represents the probability amplitude for an electron starting in the *lower-energy* eigenstate in the left lead and arriving in the lower-energy right (left) lead eigenstate if $\ell = 0$, or in the higher-energy right (left) lead eigenstate if $\ell = 1$. Contrarily, $[t_E]_{\ell,1}$ (resp. $[r_E]_{\ell,1}$) represents the probability amplitude for an electron starting in the higher-energy left lead eigenstate and arriving in the lower-energy right (left) lead eigenstate if $\ell=0$, or in the higher-energy right (left) lead eigenstate if $\ell = 1$. With these definitions, current conservation is ensured by the unitarity relation

$$r_E^{\dagger} r_E + t_E^{\dagger} t_E = 1 , \qquad (11)$$

(see Appendix A).

In the single-channel regime the injection energy E is larger than the lowest eigenvalue in the leads but smaller than their highest eigenvalue, i.e.

$$E_{\rm Z}^{(1)} = E_{\rm Z} > E > -E_{\rm Z} = E_{\rm Z}^{(0)}$$
 (12)

Under this condition only the lowest band supports electrons far from the scattering region. In this case t_E and r_E can still be defined as in (10), but the only elements associated with the low-energy eigenstates contribute to the current. Specifically, the term $[t_E]_{0,0}$ which represents the probability amplitude for an electron starting in the lower-energy eigenstate in the left lead and arriving in the lower-energy right lead eigenstate, and the element $[r_E]_{0.0}$, which represents the reflection amplitude for the same eigenstate. In this case, the current conservation identity (11) simplifies to:

$$|[r_E]_{0,0}|^2 + |[t_E]_{0,0}|^2 = 1$$
. (13)

SOLVING THE SCATTERING PROBLEM III.

To compute the values of the matrices t_E and r_E we need to explicitly find a spinor wave-function $|\psi_y^{(E)}\rangle$ which solves Eq. (6) for all y, and used it to identifying the coefficients $A_E^{(\ell)}$, $R_E^{(\ell)}$, and $T_E^{(\ell)}$ that enters in Eq. (7). For this purpose, following Ref. [10], we expand $|\psi_u^{(E)}\rangle$ w.r.t. the local eigenstates (3) of the spin operator \hat{h}_y , i.e.

$$|\psi_y^{(E)}\rangle = \sum_{\ell=0,1} C_y^{(\ell)} |\phi_{n_y}^{(\ell)}\rangle ,$$
 (14)

with $C_y^{(\ell)} := \langle \phi_{n_y}^{(\ell)} | \psi_y^{(E)} \rangle$ being (coordinate-dependent) complex probabilities amplitudes. With this choice Eq. (6) assumes the form

$$(\partial_y + K_y)^2 \boldsymbol{C}_y + \frac{2m}{\hbar^2} (E\mathbb{1} - \Omega_y) \boldsymbol{C}_y = 0 , \qquad (15)$$

where $C_y := (C_y^{(0)}, C_y^{(1)})^T$ is the column vector of coefficients $C_y^{(\ell)}$, Ω_y is a 2×2 diagonal matrix whose elements are the instantaneous eigenvalues in Eq. (3),

$$[\Omega_y]_{\ell,\ell'} := E_{Z_y}^{(\ell)} \delta_{\ell,\ell'} , \qquad (16)$$

and finally K_y is the 2×2 Berry matrix [20] of the process, whose elements are defined as

$$[K_y]_{\ell,\ell'} := \langle \phi_{\mathbf{n}_y}^{(\ell)} | \partial_y \phi_{\mathbf{n}_y}^{(\ell')} \rangle. \tag{17}$$

By construction K_y is a skew-matrix which assumes zero value in the leads and varies continuously at the interface with the scattering region, i.e.

$$K_y = -K_y^{\dagger}, \qquad (18)$$

$$K_y = 0, \quad \forall y \notin]y_{\rm L}, y_{\rm R}[. \qquad (19)$$

$$K_y = 0$$
, $\forall y \notin [y_L, y_R]$. (19)

We stress that the second request is less demanding than it might initially appear. This is due to the fact that, at large distances from the scattering region, the magnetic field becomes constant, taking the values $B_{\rm L}$ and $B_{\rm R}$. Consequently, we can enforce condition (19) by simply

redefining the boundaries of the scattering region as

$$y_{\rm L} \to y_{\rm L}^- := y_{\rm L} - \epsilon , \qquad y_{\rm R} \to y_{\rm R}^+ := y_{\rm R} + \epsilon , \quad (20)$$

with $\epsilon > 0$ is an infinitesimal positive shift. This regularization allows us to accommodate configurations in which $\boldsymbol{B}(y)$ exhibits an explicit discontinuity at the borders of the scattering region. The matrix K_y defines the Berry operator of the model via the following unitary transformation

$$\mathcal{U}_{y_1 \to y_2} := \overleftarrow{\exp} \left\{ - \int_{y_1}^{y_2} dy K_y \right\} , \qquad (21)$$

where $y_1 \leq y_2$, and $\exp[\cdots]$ indicates path ordering of the operators product. As discussed in Appendix A, setting $D_y := \partial_y C_y$ the first derivative of the vector C_y , the continuity constraint (19) allows us to formally integrate Eq. (15) producing the identity

$$\begin{bmatrix} \boldsymbol{C}_{y_{\mathrm{R}}} \\ \boldsymbol{D}_{y_{\mathrm{R}}} \end{bmatrix} = \Gamma_{y_{\mathrm{L}} \to y_{\mathrm{R}}}^{(E)} \begin{bmatrix} \boldsymbol{C}_{y_{\mathrm{L}}} \\ \boldsymbol{D}_{y_{\mathrm{L}}} \end{bmatrix} , \qquad (22)$$

with $\Gamma_{y_L \to y_R}^{(E)}$ the generalized transfer matrix of the process.

Factorizing out the Berry operator contribution, Eq. (22) can be expressed as

$$\Gamma_{y_{\mathbf{L}} \to y_{\mathbf{R}}}^{(E)} := \begin{bmatrix} \mathcal{U}_{y_{\mathbf{L}} \to y_{\mathbf{R}}} & 0\\ 0 & \mathcal{U}_{y_{\mathbf{L}} \to y_{\mathbf{R}}} \end{bmatrix} \tilde{\Gamma}_{y_{\mathbf{L}} \to y_{\mathbf{R}}}^{(E)}, \quad (23)$$

with the energy dependent term

$$\tilde{\Gamma}_{y_{\rm L} \to y_{\rm R}}^{(E)} := \overleftarrow{\exp} \left\{ \int_{y_{\rm L}}^{y_{\rm R}} dy \tilde{\mathcal{M}}_y^{(E)} \right\} , \qquad (24)$$

generated by the 4×4 block matrix

$$\tilde{\mathcal{M}}_{y}^{(E)} := \begin{bmatrix} 0 & \mathbb{1} \\ \frac{2m}{\hbar^{2}} (\tilde{\Omega}_{y} - E \mathbb{1}) & 0 \end{bmatrix} , \quad \tilde{\Omega}_{y} := \mathcal{U}_{y_{L} \to y}^{\dagger} \Omega_{y} \mathcal{U}_{y_{L} \to y} .$$

$$(25)$$

The matrix $\tilde{\mathcal{M}}_y^{\dagger(E)}$ plays a crucial role in the scattering problem. Specifically, as demonstrated in Appendix B 1, it guarantees current conservation (11) through the symmetry relation:

$$\tilde{\mathcal{M}}_{y}^{\dagger(E)} \begin{bmatrix} 0 & \mathbb{1} \\ -\mathbb{1} & 0 \end{bmatrix} + \begin{bmatrix} 0 & \mathbb{1} \\ -\mathbb{1} & 0 \end{bmatrix} \tilde{\mathcal{M}}_{y}^{(E)} = 0.$$
 (26)

Recalling Eq. (7) we can write

$$\begin{bmatrix} C_{y_{L}} \\ D_{y_{L}} \end{bmatrix} = \begin{pmatrix} A_{E}^{(0)} e^{ik_{E}^{(0)} y_{L}} + R_{E}^{(0)} e^{-ik_{E}^{(0)} y_{L}} \\ A_{E}^{(1)} e^{ik_{E}^{(1)} y_{L}} + R_{E}^{(1)} e^{-ik_{E}^{(1)} y_{L}} \\ A_{E}^{(0)} (A_{E}^{(0)} e^{ik_{E}^{(0)} y_{L}} - R_{E}^{(0)} e^{-ik_{E}^{(0)} y_{L}}) \\ ik_{E}^{(0)} (A_{E}^{(0)} e^{ik_{E}^{(0)} y_{L}} - R_{E}^{(0)} e^{-ik_{E}^{(0)} y_{L}}) \\ ik_{E}^{(1)} (A_{E}^{(1)} e^{ik_{E}^{(1)} y_{L}} - R_{E}^{(1)} e^{-ik_{E}^{(1)} y_{L}}) \end{pmatrix},$$

$$\begin{bmatrix} C_{y_{R}} \\ D_{y_{R}} \end{bmatrix} = \begin{pmatrix} T_{E}^{(0)} e^{ik_{E}^{(0)} y_{R}} \\ T_{E}^{(1)} e^{ik_{E}^{(1)} y_{R}} \\ ik_{E}^{(0)} T_{E}^{(0)} e^{ik_{E}^{(0)} y_{R}} \\ ik_{E}^{(1)} T_{E}^{(1)} e^{ik_{E}^{(1)} y_{R}} \end{pmatrix},$$

$$(27)$$

which replaced in Eq. (22), leads to a set of 4 linear identities that link the amplitudes $T_E^{(\ell)}$ and $R_E^{(\ell)}$ to the input amplitudes $A_E^{(\ell)}$. In conjunction with Eq. (10) this results in two linear equations for t_E and r_E , i.e.

$$\begin{cases} W^{-1}t_{E}W = F_{R}^{\dagger}\mathcal{U}_{y_{L}\to y_{R}}\left(X_{0,0} + iX_{0,1}V\right)F_{L} \\ +F_{R}^{\dagger}\mathcal{U}_{y_{L}\to y_{R}}\left(X_{0,0} - iX_{0,1}V\right)F_{L}^{\dagger}W^{-1}r_{E}W, \end{cases}$$

$$iVW^{-1}t_{E}W = F_{R}^{\dagger}\mathcal{U}_{y_{L}\to y_{R}}\left(X_{1,0} + iX_{1,1}V\right)F_{L} \\ +F_{R}^{\dagger}\mathcal{U}_{y_{L}\to y_{R}}\left(X_{1,0} - iX_{1,1}V\right)F_{L}^{\dagger}W^{-1}r_{E}W,$$
(28)

where W, V, and $F_{\rm L,R}$ are 2×2 diagonal matrices defined in Eqs. (A2) and (A4) of Appendix A 1, and $X_{0,0}$, $X_{0,1}$, $X_{1,0}$, $X_{1,1}$ the 2×2 blocks components of $\tilde{\Gamma}_{y_{\rm L}\to y_{\rm R}}^{(E)}$ defined in Eq. (B12). Once determined the path-ordered exponent (24), Eq. (28) can be numerically inverted obtaining t_E and r_E . We note that, at odds with Ref. [10], the scattering amplitudes are now calculated exactly at any given energy E.

IV. SPECIAL REGIMES

The analysis allows for a fully analytical treatment in at least three distinct regimes. The first is the asymptotic limit where E is significantly larger than any other energy scale in the model. The second occurs when the variation of the magnetic field within the scattering region is minimal. The third regime arises when the magnetic field in the scattering region is piecewise constant.

A. Large energy limit

Let us first consider the case where the particle energy is much larger than the Zeeman energy splitting in the wire, i.e.

$$E \gg \Delta E_{\rm Z}^{({\rm max})} := \max_{y} (E_{\rm Z}_{y}^{(1)} - E_{\rm Z}_{y}^{(0)})$$

= $2g\mu_{B} \max_{y} |\mathbf{B}(y)|$. (29)

In this regime one has that

$$k_E^{(0)} \simeq k_E^{(1)} \simeq k_E := \sqrt{2mE}/\hbar ,$$
 (30)

and we can disregard the spatial modulation of $\tilde{\mathcal{M}}_y^{(E)}$ induced by the instantaneous Zeeman eigen-energy term $2m\tilde{\Omega}_y/\hbar^2$,

$$\tilde{\mathcal{M}}_{y}^{(E)}\Big|_{E\gg\Delta E_{z}^{(\max)}} \simeq \mathcal{M}_{E} := \begin{bmatrix} 0 & \mathbb{1} \\ -k_{E}^{2}\mathbb{1} & 0 \end{bmatrix}.$$
(31)

Accordingly the path-ordered exponent associated with such operator can be explicitly computed obtaining

$$\tilde{\Gamma}_{y_{L} \to y_{R}}^{(E)} \Big|_{E \gg \Delta E_{Z}^{(\text{max})}} \simeq \exp\{\mathcal{M}_{E} L\} \tag{32}$$

$$= \begin{bmatrix} \cos(k_{E} L) \mathbb{1} & k_{E}^{-1} \sin(k_{E} L) \mathbb{1} \\ -k_{E} \sin(k_{E} L) \mathbb{1} & \cos(k_{E} L) \mathbb{1} \end{bmatrix},$$

where $L := y_R - y_L$ represents the length of the scattering region. By replacing the above identity in Eq. (22) and solving for $T_E^{(\ell)}$ and $R_E^{(\ell)}$, this leads finally to

$$t_E \Big|_{E \gg \Delta E_{\mathbf{Z}}^{(\text{max})}} \simeq \mathcal{U}_{y_{\mathbf{L}} \to y_{\mathbf{R}}}, \qquad r_E \Big|_{E \gg \Delta E_{\mathbf{Z}}^{(\text{max})}} \simeq 0 , \quad (33)$$

i.e. the transmission matrix is equal to the Berry operator, with no reflection (see Appendix C for details).

Equation (33) has a significant implication when one considers that, in the large-energy limit, the scattering process should have a negligible effect on the spin of the particle. Physically, this can be understood through an analogy with dynamical quenches: a high-energy particle propagating from left to right along the wire encounters a sudden, abrupt change in the external magnetic field. This rapid variation leaves the spin invariant and induces no reflections. If one adopts this ansatz, as detailed in App. C1, Eq. (33) leads to the following key identity

$$[\mathcal{U}_{y_{\mathrm{L}}\to y_{\mathrm{R}}}]_{\ell',\ell} = \langle \phi_{\mathbf{n}_{\mathrm{R}}}^{(\ell')} | \phi_{\mathbf{n}_{\mathrm{L}}}^{(\ell)} \rangle , \qquad (34)$$

In Sec. V, we will provide a proof of Eq. (34) for the special case where the variation of the magnetic field along the 1D wire is constrained on a fixed plane. Additionally, we will present an argument that extends the result to the general case. The identity (34) is a remarkable result: it reveals that the Berry operator $\mathcal{U}_{y_L \to y_R}$ can be determined analytically and depends solely on the magnetic field's components at the boundaries, hence reducing to a purely topological form. Crucially, it is independent of the magnetic field's behavior in the scattering region or the length $L = y_R - y_L$. Notably, this result predicts that if the magnetic fields at the left and right leads are identical (i.e. $n_R = n_L$), the Berry operator transformation reduces to the identity.

B. Infinitesimal scattering region limit

When the variation of the magnetic field inside the scattering region is sufficiently small the path-ordered exponent in Eq. (22) can be approximated by a regular exponential

$$\tilde{\Gamma}_{y_{\rm L} \to y_{\rm R}}^{(E)} \simeq \exp \left\{ \int_{y_{\rm L}}^{y_{\rm R}} dy \tilde{\mathcal{M}}_{y}^{(E)} \right\} = \mathcal{D}_{\rm L}(Q_E) , \quad (35)$$

where Q_E is the Hermitian matrix

$$Q_E := \frac{2m}{\hbar^2} \left(E \mathbb{1} - \int_{y_{\rm L}}^{y_{\rm R}} dy \tilde{\Omega}_y / L \right) , \qquad (36)$$

and

$$\mathcal{D}_{L}(Q_{E}) := \begin{bmatrix} \cos(\sqrt{Q_{E}}L) & \frac{1}{\sqrt{Q_{E}}}\sin(\sqrt{Q_{E}}L) \\ -\sqrt{Q_{E}}\sin(\sqrt{Q_{E}}L) & \cos(\sqrt{Q_{E}}L) \end{bmatrix} , \quad (37)$$

(see App. D for details). Observe in particular, that for infinitesimally short scattering regions (i.e. $L \to 0$), the matrix $\mathcal{D}_{\mathrm{L}}(Q_E)$, and hence $\tilde{\Gamma}_{y_{\mathrm{L}}\to y_{\mathrm{R}}}^{(E)}$, reduces to the identity. However, this behavior does not necessarily extend to the Berry operator. Specifically, as long as the boundary conditions at the edges of the scattering region are preserved in the $L \to 0$ limit, Eq. (34) remains applicable and can assign a non-trivial value to $\mathcal{U}_{y_{\mathrm{L}}\to y_{\mathrm{R}}}$. These special conditions are satisfied when the magnetic field $\boldsymbol{B}(y)$ undergoes an abrupt transition from $\boldsymbol{B}_{\mathrm{L}}$ to $\boldsymbol{B}_{\mathrm{R}}$ at a single point $y_{\mathrm{L}} = y_{\mathrm{R}} = y_{\star}$ of the 1D wire. Under such circumstances, leveraging the preceding analysis, we can hence write

$$\left. \Gamma_{y_{\rm L} \to y_{\rm R}}^{(E)} \right|_{L=0} = \begin{bmatrix} \mathcal{U}_{y_{\star}} & 0\\ 0 & \mathcal{U}_{y_{\star}} \end{bmatrix}, \tag{38}$$

with $\mathcal{U}_{y_{\star}} := \mathcal{U}_{y_{\star}^{-} \to y_{\star}^{+}}$ the Berry operator acquired when crossing the discontinuity point. Replaced into Eq. (28) this implies

$$t_{E}\Big|_{L=0} = 2W^{-1}\mathcal{U}_{y_{\star}}W\frac{1}{W\mathcal{U}_{y_{\star}}^{\dagger}W^{-2}\mathcal{U}_{y_{\star}}W+1},$$

$$r_{E}\Big|_{L=0} = \frac{W\mathcal{U}_{y_{\star}}^{\dagger}W^{-2}\mathcal{U}_{y_{\star}}W-1}{W\mathcal{U}_{y_{\star}}^{\dagger}W^{-2}\mathcal{U}_{y_{\star}}W+1},$$
(39)

which represents the transfer and reflection matrices through the discontinuity (as shown in App. D for $E \to \infty$ these solutions behave as predicted by Eq. (33)).

C. Piecewise constant field regime

When the magnetic field is a piecewise constant function the operator $\Gamma^{(E)}_{y_{\rm L} \to y_{\rm R}}$ can be expressed as an ordered product of simpler terms. Specifically, let us assume that there exists a collection of ordered points

$$y_0 = y_L < y_1 < y_2 < \dots < y_{N-1} < y_N = y_R$$
, (40)

that identify a collection of N non-overlapping intervals $I_{j,j+1} :=]y_j, y_{j+1}[$ over which the magnetic field (and hence Ω_y), take constant values. Under this condition we can write

$$\Gamma_{y_{L} \to y_{R}}^{(E)} = \begin{bmatrix} \mathcal{U}_{N} & 0 \\ 0 & \mathcal{U}_{N} \end{bmatrix} \mathcal{D}_{L_{N-1}}(Q_{E}^{(N-1)}) \cdots$$

$$\cdots \begin{bmatrix} \mathcal{U}_{2} & 0 \\ 0 & \mathcal{U}_{2} \end{bmatrix} \mathcal{D}_{L_{1}}(Q_{E}^{(1)}) \begin{bmatrix} \mathcal{U}_{1} & 0 \\ 0 & \mathcal{U}_{1} \end{bmatrix} \mathcal{D}_{L_{0}}(Q_{E}^{(0)}) \begin{bmatrix} \mathcal{U}_{0} & 0 \\ 0 & \mathcal{U}_{0} \end{bmatrix},$$
(41)

where for all $j \in \{0, 1, \dots, N\}$, $\mathcal{U}_j := \mathcal{U}_{y_j^- \to y_j^+}$ represents the Berry operator transformation one gets when crossing the discontinuity point y_j , $\mathcal{D}_{L_j}(\dots)$ is the matrix function defined in Eq. (37), and finally

$$L_{j} := y_{j+1} - y_{j} ,$$

$$Q_{E}^{(j)} := \frac{2m}{\hbar^{2}} (E\mathbb{1} - \Omega_{j}) ,$$
(42)

with Ω_j being the value of Ω_y in the interval $I_{j,j+1}$. The derivation of Eq. (41) is provided in App. E. Notably, by factoring out the total Berry operator contribution as defined in (23), the right-hand side of Eq. (41) can be equivalently rewritten in the form:

$$\Gamma_{y_{L} \to y_{R}}^{(E)} = \begin{bmatrix} \mathcal{U}_{y_{L} \to y_{R}} & 0 \\ 0 & \mathcal{U}_{y_{L} \to y_{R}} \end{bmatrix} \tilde{\mathcal{D}}_{L_{N-1}}(Q_{E}^{(N-1)}) \cdots \\
\cdots \tilde{\mathcal{D}}_{L_{1}}(Q_{E}^{(1)}) \tilde{\mathcal{D}}_{L_{0}}(Q_{E}^{(0)}) ,$$
(43)

where now

$$\tilde{\mathcal{D}}_{L_{j}}(Q_{E}^{(j)}) :=
\begin{bmatrix}
\mathcal{U}_{y_{L} \to y_{j}}^{\dagger} & 0 \\
0 & \mathcal{U}_{y_{L} \to y_{j}}^{\dagger}
\end{bmatrix} \mathcal{D}_{L_{j}}(Q_{E}^{(j)}) \begin{bmatrix}
\mathcal{U}_{y_{L} \to y_{j}} & 0 \\
0 & \mathcal{U}_{y_{L} \to y_{j}}
\end{bmatrix},$$

with

$$\mathcal{U}_{y_{\rm L}\to y_j} = \mathcal{U}_j \cdots \mathcal{U}_1 \mathcal{U}_0 , \qquad (45)$$

the Berry operator accumulated moving from $y_{\rm L}^-$ to y_j^+ . As a particular application let us consider the special case of a piecewise constant scattering region where

$$\mathbf{B}(y) = 0 \qquad \forall y \in]y_{L}, y_{R}[. \tag{46}$$

Since in this case $Q_E^{(0)} = \frac{2m}{\hbar^2} E \mathbb{1}$, Eq. (41) reduces to

$$\Gamma_{y_{\rm L}\to y_{\rm R}}^{(E)} = \begin{bmatrix} \cos(k_E L)\mathcal{U}_{y_{\rm L}\to y_{\rm R}} & k_E^{-1}\sin(k_E L)\mathcal{U}_{y_{\rm L}\to y_{\rm R}} \\ -k_E\sin(k_E L)\mathcal{U}_{y_{\rm L}\to y_{\rm R}} & \cos(k_E L)\mathcal{U}_{y_{\rm L}\to y_{\rm R}} \end{bmatrix}.$$

$$(47)$$

We finally observe that the identity (41), together with Eq. (35), allows us to derive approximate solutions for $\Gamma_{y_L \to y_R}^{(E)}$ for arbitrary choices of \boldsymbol{B}_y . Specifically, a finite-length scattering region can be divided into N equally spaced segments $[y_j, y_{j+1}[$ (with $j \in \{0, 1, ..., N-1\},$ $y_0 = y_L$ and $y_N = y_R$) of length $\Delta y := L/N$. Provided that Δy is sufficiently small to ensure the validity

of Eq. (35) across all segments, Eq. (41) can then be employed as a well-defined numerical procedure for solving the scattering problem.

V. BERRY OPERATOR

To compute the Berry operator transformation (21) we begin by considering the special case where the variation of the magnetic field along the 1D wire is restricted to a fixed plane. Under this assumption, the 3D vector $\boldsymbol{n}(y)$, which specifies the orientation of the magnetic field $\boldsymbol{B}(y)$, can be expressed in terms of a single polar angle θ_y as:

$$\boldsymbol{n}(y) := \sin(\theta_y)\boldsymbol{n}_1 + \cos(\theta_y)\boldsymbol{n}_3 , \qquad (48)$$

with n_1 and n_3 are orthonormal vectors. The Zeeman eigenvectors (3) can hence be expressed as

$$\begin{cases} |\phi_{\boldsymbol{n}(y)}^{(0)}\rangle = \cos\left(\frac{\theta_{y}}{2}\right)|\downarrow\rangle - \sin\left(\frac{\theta_{y}}{2}\right)|\uparrow\rangle = e^{-i(\theta_{y}/2)\hat{\sigma}_{\boldsymbol{n}_{2}}}|\downarrow\rangle , \\ |\phi_{\boldsymbol{n}(y)}^{(1)}\rangle = \cos\left(\frac{\theta_{y}}{2}\right)|\uparrow\rangle + \sin\left(\frac{\theta_{y}}{2}\right)|\downarrow\rangle = e^{-i(\theta_{y}/2)\hat{\sigma}_{\boldsymbol{n}_{2}}}|\uparrow\rangle , \end{cases}$$
(49)

with $|\downarrow\rangle:=|\phi_{\boldsymbol{n_3}}^{(0)}\rangle$ and $|\uparrow\rangle:=|\phi_{\boldsymbol{n_3}}^{(1)}\rangle$ the eigenvectors of the Pauli operator $\hat{\sigma}_{\boldsymbol{n_3}}:=\boldsymbol{n_3}\cdot\hat{\sigma}$ associated to the eigenvalues -1 and 1 respectively, and $\hat{\sigma}_{\boldsymbol{n_2}}:=\boldsymbol{n_2}\cdot\hat{\boldsymbol{\sigma}}$ the Pauli operator associated to the vector $\boldsymbol{n_2}:=\boldsymbol{n_3}\times\boldsymbol{n_1}$ (expressed in matrix form in the representation for which $|\uparrow\rangle:=\begin{pmatrix}1\\0\end{pmatrix}$ and $|\downarrow\rangle:=\begin{pmatrix}0\\1\end{pmatrix}$, $\sigma_{\boldsymbol{n_2}}$ is just the matrix $\begin{pmatrix}0&-i\\i&0\end{pmatrix}$). From Eq. (49) it follows

$$\begin{cases}
|\partial_y \phi_{\mathbf{n}(y)}^{(0)}\rangle = -(\partial_y \theta_y) |\phi_{\mathbf{n}(y)}^{(1)}\rangle / 2, \\
|\partial_y \phi_{\mathbf{n}(y)}^{(1)}\rangle = (\partial_y \theta_y) |\phi_{\mathbf{n}(y)}^{(0)}\rangle / 2,
\end{cases} (50)$$

so that the Berry matrix (17) becomes

$$K_y = (\partial_y \theta_y) \begin{pmatrix} 0 & 1/2 \\ -1/2 & 0 \end{pmatrix} = i(\partial_y \theta_y) \sigma_{n_2}/2.$$
 (51)

Now note that Eq. (51) implies that the commutator $[K_y, K_{y'}] = 0$ for all y and y'. Since the ordered exponential simplifies to a standard exponential, the Berry operator can therefore be evaluated analytically, resulting in the following expression:

$$\mathcal{U}_{y_{L} \to y} = \exp \left[-(i/2) \int_{\theta_{y_{L}}}^{\theta_{y}} dy \, (\partial_{y} \theta_{y}) \sigma_{\mathbf{n}_{2}} \right]$$
$$= \exp \left[-i \left(\frac{\theta_{y} - \theta_{y_{L}}}{2} \right) \sigma_{\mathbf{n}_{2}} \right], \tag{52}$$

which in particular, for $y = y_R$ yields

$$\mathcal{U}_{y_{\mathrm{L}}\to y_{\mathrm{R}}} = \exp\left[-i(\frac{\alpha}{2})\sigma_{n_{2}}\right] = \begin{pmatrix} \cos(\alpha/2) & -\sin(\alpha/2) \\ \sin(\alpha/2) & \cos(\alpha/2) \end{pmatrix},$$
(53)

with $\alpha := \theta_{y_R} - \theta_{y_L}$. Using Eq. (49) one can easily verify that the matrix elements of Eq. (53) matches exactly

with the prediction of Eq. (34). We can hence conclude that such an identity can be explicitly proved for the special cases where the n(y) evolve an a 2D plane as in (48). Extending this result for arbitrary trajectories of n(y) can be achieved by employing the same strategy outlined at the end of Sec. IVB for the numerical evaluation of $\exp\left\{\int_{y_{\rm L}}^{y_{\rm R}} dy \tilde{\mathcal{M}}_y^{(E)}\right\}$. Specifically this time we decompose the scattering region into N equally spaced segments $[y_j, y_{j+1}[$ (with $j \in \{0, 1, ..., N-1\}, y_0 = y_{\rm L}$ and $y_N = y_{\rm R}$) of the length $\Delta y = L/N$ so that

$$\mathcal{U}_{y_1 \to y_2} = \mathcal{U}_{y_{N-1} \to y_N} \cdots \mathcal{U}_{y_2 \to y_3} \mathcal{U}_{y_1 \to y_2} \mathcal{U}_{y_0 \to y_1}$$
. (54)

Now, assume that the length $\Delta y = L/N$ is sufficiently small so that, within each interval, the evolution of $\boldsymbol{n}(y)$ can be approximated as occurring on a 2D plane. More precisely, for each j, we assume that there exists a couple of orthonormal axis $\boldsymbol{n}_1^{(j)}$ and $\boldsymbol{n}_3^{(j)}$, along with a function $\theta_y^{(j)}$ such that

$$\boldsymbol{n}(y) \simeq \sin(\theta_y^{(j)}) \boldsymbol{n}_1^{(j)} + \cos(\theta_y^{(j)}) \boldsymbol{n}_3^{(j)}, \ \forall y \in [y_j, y_{j+1}].$$
(55)

By invoking (53) we can hence evaluate the individual terms in the product (54) via (34). Specifically for all j we have $[\mathcal{U}_{y_j \to y_{j+1}}]_{\ell',\ell} = \langle \phi_{\boldsymbol{n}_{j+1}}^{(\ell')} | \phi_{\boldsymbol{n}_j}^{(\ell)} \rangle$. Note then that this property implies that

$$[\mathcal{U}_{y_{j+1} \to y_{j+2}} \mathcal{U}_{y_{j} \to y_{j+1}}]_{\ell',\ell}$$

$$= \sum_{\ell'' = \{0,1\}} [\mathcal{U}_{y_{j+1} \to y_{j+2}}]_{\ell'\ell''} [\mathcal{U}_{y_{j} \to y_{j+1}}]_{\ell'',\ell}$$

$$= \sum_{\ell'' = \{0,1\}} \langle \phi_{\boldsymbol{n}_{j+2}}^{(\ell')} | \phi_{\boldsymbol{n}_{j+1}}^{(\ell'')} \rangle \langle \phi_{\boldsymbol{n}_{j+1}}^{(\ell'')} | \phi_{\boldsymbol{n}_{j}}^{(\ell)} \rangle$$

$$= \langle \phi_{\boldsymbol{n}_{j+2}}^{(\ell')} | \phi_{\boldsymbol{n}_{j}}^{(\ell)} \rangle . \tag{56}$$

which used in (54) allows us to conclude that

$$[\mathcal{U}_{y_{\rm L}\to y_{\rm R}}]_{\ell',\ell} = \langle \phi_{\boldsymbol{n}_N}^{(\ell')} | \phi_{\boldsymbol{n}_0}^{(\ell)} \rangle = \langle \phi_{\boldsymbol{n}_{\rm R}}^{(\ell')} | \phi_{\boldsymbol{n}_{\rm L}}^{(\ell)} \rangle , \qquad (57)$$

hence proving (34).

VI. EXAMPLES

In this section we apply the method developed in Sec. III to two different examples under the assumption that along the 1D wire the Zeeman field varies continuously in a fixed 2D plane determined by the directions n_1 and n_3 as indicated in Eq. (48), i.e.

$$\mathbf{B}(y) = B_1(y)\mathbf{n}_1 + B_3(y)\mathbf{n}_3. \tag{58}$$

A. Scheme I

Consider the scenario depicted in panel a) of Fig. 1, where the Zeeman field in the two leads has the same

magnitude, is directed along the some axis n_3 , but with opposite orientations, i.e.

$$B_{\rm L} = B_0 \, n_3 \; , \qquad B_{\rm R} = -B_0 \, n_3 \; , \tag{59}$$

corresponding to set $n_L = n_3$ and $n_R = -n_3$. Adopting the notation of Eq. (49), this in particular implies

$$|\phi_{y_{\rm L}}^{(0)}\rangle = |\phi_{n_3}^{(0)}\rangle = |\downarrow\rangle = |\phi_{-n_3}^{(1)}\rangle = |\phi_{y_{\rm R}}^{(1)}\rangle ,$$
 (60)

$$|\phi_{y_{\text{L}}}^{(1)}\rangle = |\phi_{n_3}^{(1)}\rangle = |\uparrow\rangle = -|\phi_{-n_3}^{(0)}\rangle = -|\phi_{y_{\text{R}}}^{(0)}\rangle$$
. (61)

To interpolate among the values (59) we define the components of the field (58) in the scattering region to have the form

$$\begin{cases} B_1(y) := \beta_0(y) B_0 \left[\sin \left((1 + 2q_2) \frac{\pi(y - y_L)}{y_R - y_L} \right) \right]^{(2 + 2q_1)}, \\ B_3(y) := B_0 \left[\cos \left((1 + 2q_2) \frac{\pi(y - y_L)}{y_R - y_L} \right) \right]^{(1 + 2q_1)}. \end{cases}$$
(62)

where q_1 and q_2 are non-negative integer numbers. In particular q_1 accounts for the sharpness of the magnetic field components: if q_1 increases, $B_1(y)$ will have support in an increasingly smaller region around the middle point of the scattering region while $B_3(y)$ will nullify in the whole scattering domain, connecting with the correct boundary conditions to the leads. Indeed, in the limiting case of $q_1 \to \infty$, this scheme reduced to the first example in App. G (magnetic wall model) with $n_{\rm L}=n_3$ and $n_{\rm R}=-n_3$. Starting from the left lead, the integer q_2 accounts for complete winding (in the n_1 - n_3 plane) of the magnetic field before ending with the correct boundary condition on the right lead, for which we need to introduce the phase function $\beta_0(y)$ (with values ± 1). In the limiting case where $q_2 \rightarrow \infty$, with magnetic field components oscillating very rapidly and having zero average, we expect the system to reduce to the magnetic wall model, illustrated in the first example of Appendix G with $n_L = n_3$ and $n_R = -n_3$. Specifically, while |B(y)| > 0 for all y, both $\partial_y B_1(y)$ and $\partial_y B_3(y)$ are zero for $y \to y_{\rm R/L}$. Consequently, we have $K_{y_{\rm L}} = K_{y_{\rm R}} = 0$, indicating that (22) is valid for use. This allow us to apply the procedure outlined in Appx. B 2 to calculate the transmission matrix t_E . Furthermore since $\lim_{y\to y_{\rm R}}\theta_y=\pi$ and $\theta_{y_{\rm L}}=0$ we obtain $\alpha=\pi$, and thus

$$\mathcal{U}_{y_{\rm L}\to y_{\rm R}} = -i\sigma_{n_2} = \begin{pmatrix} 0 & -1\\ 1 & 0 \end{pmatrix} . \tag{63}$$

Alternatively, this result can be derived using (34) and (61). We next compute the probability $P_E^{(\downarrow \mapsto \uparrow)}$ for an electron injected in the left lead in the lower-energy state $|\phi_{y_{\rm L}}^{(0)}\rangle$ (corresponding to the spin down state $|\downarrow\rangle$) to be transmitted in the lower-energy state in the right lead $|\phi_{y_{\rm L}}^{(0)}\rangle$ (corresponding to the spin up state $|\uparrow\rangle$), i.e.

$$P_E^{(\downarrow \mapsto \uparrow)} := |[t_E]_{0,0}|^2. \tag{64}$$

This, along with the corresponding reflection probability $|[r_E]_{0,0}|^2$, is the only scattering process which is allowed when we are in the single-channel regime (12). Indeed, for $E < E_{\rm Z}$, no higher-energy states are available for transport, as E is below the bottom of the higherenergy band. In contrast, in the two-channel regime (9), where $E > E_{\rm Z}$, we can also define two more transmission probabilities. Specifically, $P_E^{(\uparrow \mapsto \downarrow)} = |[t_E]_{1,1}|^2$ represents the probability that an electron injected in the left lead in the higher-energy state (corresponding to the spin up) to be transmitted in the higher-energy state in the right lead (corresponding to the spin down). Similarly, $P_E^{(\downarrow \rightarrow \downarrow)} = |[t_E]_{1,0}|^2$ is the probability that an electron injected in the left lead in the low-energy state (spin-down) is transmitted into the higher-energy state in the right lead (spin down). Finally, we have the $P_E^{(\uparrow \mapsto \uparrow)} = |[t_E]_{0,1}|^2$, which corresponds to an electron injected in the left lead in the lower-energy state (spin-up) being transmitted into the lower-energy state in the right lead (spin-up). In Fig. 2 we plot the transmission probabilities defined above as functions of E (in units of the Zeeman energy splitting $E_{\rm Z}$) for a wire of length $L = 3L_{\rm Z}$, where $L_{\rm Z} := \sqrt{\hbar^2/(2mE_{\rm Z})}$ is the Zeeman length. The various panels refer to different values of the parameters q_1 and q_2 . In the main panels, the energy ranges between $-E_{\rm Z}$ and $5E_{\rm Z}$, covering both the single- and two-channel regime, while in the insets we focus only on the two-channel regime, considering energies within the range $[E_{\rm Z}, 10E_{\rm Z}]$. The green curve represents the probability $P_E^{(\downarrow \mapsto \uparrow)}$, the red curve represents $P_E^{(\uparrow \mapsto \downarrow)}$, and the orange curve represents $P_E^{(\downarrow \mapsto \downarrow)}$. Interestingly, $P_E^{(\downarrow \mapsto \downarrow)}$ is always equal to $P_E^{(\uparrow \mapsto \uparrow)}$ (as we shall see in the following when E is sufficiently larger, such behaviour follows directly from Eqs. (53) and (33)). Let us first discuss panel a), relative to $q_1 = 0$ and $q_2 = 0$. The numerical results show that, in the single-channel regime, the only transmission probability that is different from zero is $P_E^{(\downarrow \mapsto \uparrow)}$, as expected. This probability increases monotonically from zero at $E = -E_Z$ (bottom of the lower band), rapidly approaching 1 (i.e. a perfect transition from the spin-down state to the spin-up state) as the energy nears $E_{\rm Z}$. For $E > E_{\rm Z}$ the green curve decreases monotonically, while the red curve, after a rapid increase, starts decrease and eventually joins the green curve at $E \simeq 2E_{\rm Z}$. Beyond this point, both $P_E^{(\downarrow \mapsto \uparrow)}$ and $P_E^{(\uparrow \mapsto \downarrow)}$ decrease to zero for sufficiently large energies (see inset). The orange curve, representing $P_E^{(\downarrow \mapsto \downarrow)}$ and $P_E^{(\uparrow \mapsto \uparrow)}$, also starts from zero for $E > E_Z$ monotonously increases and eventually reaching 1 for large values of E (see inset). The behavior of the transmission probabilities for $E \gg E_{\rm Z}$ is as expected, since, according to Eq. (33), the transmission matrix is completely determined by the Berry operator in Eq. (63). As a result, we have $P_E^{(\downarrow \mapsto \uparrow)} = P_E^{(\uparrow \mapsto \downarrow)} = 0$ and $P_E^{(\uparrow \mapsto \uparrow)} = P_E^{(\downarrow \mapsto \downarrow)} = 1$. In this regime, the reflection amplitudes are suppressed, and the particle retains the same spin value of the incoming field as the incoming state. Notably, $P_E^{(\downarrow \mapsto \uparrow)}$ and $P_E^{(\uparrow \mapsto \downarrow)}$ become virtually equal for an energy as small as $E \simeq 2E_{\rm Z}$. Notably, even at $E \simeq 6E_{\rm Z}$, both $P_E^{(\downarrow \mapsto \downarrow)}$ and $P_E^{(\uparrow \mapsto \uparrow)}$ reach a value of 0.9, indicating that 90% inversion of the input energy band population has been achieved. For example, electrons entering the left lead in the lowenergy band will exit the right lead in the opposite band with 90% probability. It is important to highlight that, due to energy conservation, this effect is accompanied by a partial conversion of the kinetic energy component into spinor energy. This conversion results in a net reduction in momentum, given by

$$\Delta k_E := k_E^{(1)} - k_E^{(0)} = -\sqrt{\frac{2mE}{\hbar^2}} \left(\sqrt{1 + \frac{E_Z}{E}} - \sqrt{1 - \frac{E_Z}{E}} \right)$$
$$\simeq -\sqrt{\frac{2mE_Z^2}{\hbar^2 E}} . \tag{65}$$

The opposite effect occurs for electrons entering the left lead in the high-energy band: with a 90% probability, they will emerge in the low-energy band on the right lead, accompanied by an increase in their kinetic energy. The net gain in momentum in this case is $|\Delta k_E|$.

By increasing the value of q_1 , for fixed $q_2 = 0$, the transmission probabilities are modified as shown in panels b) and c). The main effect of increasing q_1 is that the probability $P_E^{(\downarrow \mapsto \downarrow)}$, see panel c), reaches more quickly the value 1 for $E > E_{\rm Z}$, i.e. the transmission ma trix is completely determined by the Berry operator. A similar effect is observed when increasing the value of q_2 , for a fixed $q_1 = 0$ [panels d) and e)]. A notable additional effect of larger values of q_2 is the significant suppression of the probability $P_E^{(\downarrow \to \uparrow)}$, even for energies $E < E_{\rm Z}$. We quantify how much the transmission matrix aligns to the Berry operator (63) as a function of the injection energy E, using the Hilbert-Schmidt distance $||A-B||_{HS} := \sqrt{\text{Tr}[(A-B)(A-B)^{\dagger}]}$. In the main panel of Fig. 3a) we plot the distance $||t_E(L) - \mathcal{U}_{y_L \to y_R}||_{HS}$ for $q_1 = 0, 1, 10$, with $q_2 = 0$. Moreover we plot the Hilbert-Schmidt distance $||t_E^{\rm I}(L) - \mathcal{U}_{y_{\rm L} \to y_{\rm R}}||_{\rm HS}$ for the magnetic wall configuration described in Appx. G with $n_{\rm L}=n_3$ and $n_{\rm R} = -n_3$, see the red dashed curve in the main panel of Fig. 3b). Then we quantify the contribution of the back scattering in the process by plotting the norm $||r_E(L)||_{HS}$ as a function og the injection energy in the inset of Fig. 3a) (the analytical behavior of $||r_E^I(L)||_{HS}$ is plotted with red dashed line). Similarly, in Fig 3a) we quantify both $||t_E(L) - \mathcal{U}_{y_L \to y_R}||_{HS}$ (main panel) and $||r_E^I(L)||_{HS}$ (inset) for $q_2 = 0, 1, 10$, with $q_1 = 0$, as a function of the injection energy E.

B. Scheme II

In this second example, we assume that the Zeeman field in the left lead and the right lead is directed along

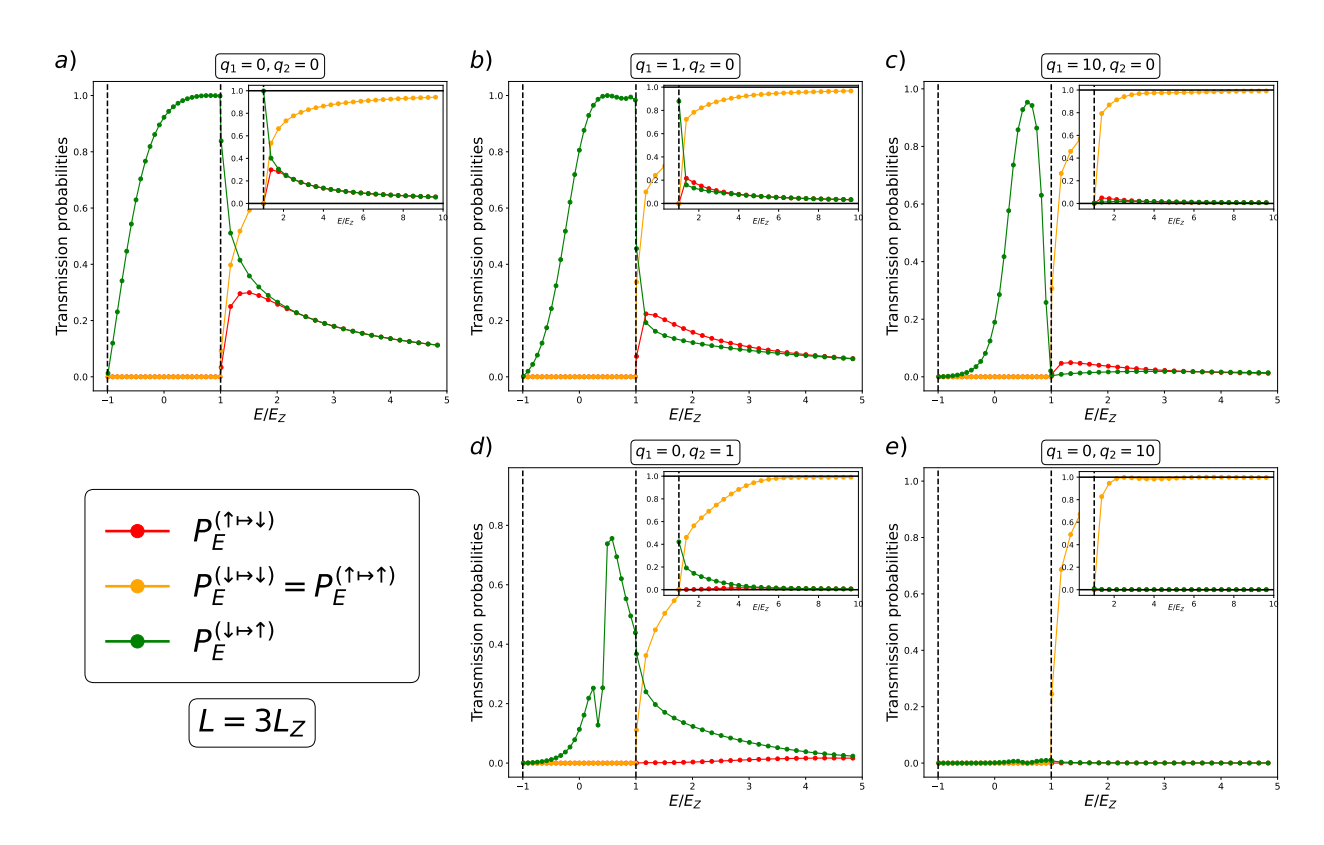


FIG. 2. Transmission probabilities as a function of injection energy for Scheme I (Sec. VIA), with $L=3L_Z$. Each panel corresponds to different values of the parameters q_1 and q_2 , which are specified at the top of each panel. The value of $L=3L_Z$ was selected because it enables nearly perfect spin flip $(P_E^{\uparrow \mapsto \downarrow} \approx 1)$ over the energy range from 0 to E_Z when both parameters are set to zero $(q_1=0, q_2=0)$, as illustrated in panel a). The insets in all plots display an extended energy range, allowing access to the high-energy limit where $E/E_Z \to \infty$. In this limit, for all cases, the red and green curves $(P_E^{\uparrow \mapsto \downarrow})$ and $(P_E^{\downarrow \mapsto \downarrow})$ approach zero, while the orange curve $(P_E^{\uparrow \mapsto \uparrow})$ approaches 1. This behavior confirms the prediction given by Eq. (C4), where the transmission matrix at large energies coincides with the Berry operator. Notably, this result is independent of q_1 and q_2 , as the Berry operator depends solely on the magnetic field components in the leads [see Eq. (53)].

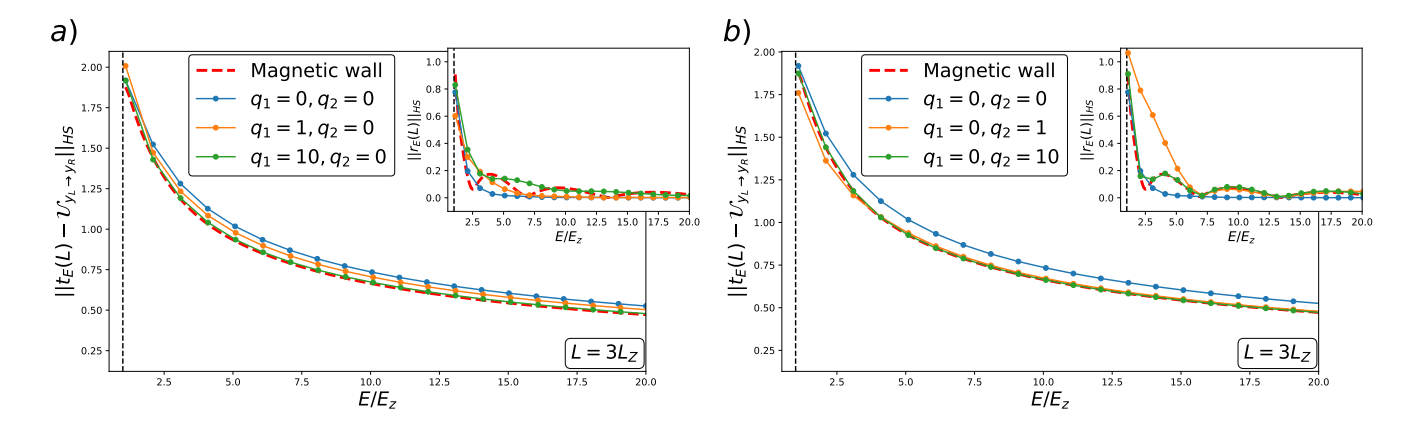


FIG. 3. Scheme I, numerical results of the Hilbert-Schmidt norms $||t_E(L) - \mathcal{U}_{y_L \to y_R}||_{\text{HS}}$ and $||r_E(L)||_{\text{HS}}$ (blue, orange, and green dotted curves) as a function of injection energy E. The dashed red lines represent the exact solution for the magnetic wall configuration in Scheme I (Appx. D), showing $||t_E^I(L) - \mathcal{U}_{y_L \to y_R}||_{\text{HS}}$ and $||r_E^I(L)||_{\text{HS}}$. In panel a) we vary q_1 ($q_1 = 0, 1, 10$) with $q_2 = 0$ fixed, while in panel b) we fixes $q_1 = 0$ and varies q_2 ($q_2 = 0, 1, 10$). In both cases, the distance between the dashed red curve and the dotted curves decreases as q_1 or q_2 increases, confirming that Scheme I (Sec. VI A) approaches the magnetic wall configuration ($n_L = n_3$, $n_R = -n_3$) in the limit $q_1 \to \infty$ (with $q_2 = 0$) or $q_2 \to \infty$ (with $q_1 = 0$), as discussed in Appx. G.

orthogonal axes. Specifically, as shown in panel b) of Fig. 1 we set

$$B_{\rm L} = B_0 \, n_3 \; , \qquad B_{\rm R} = B_0 \, n_1 \; . \tag{66}$$

which corresponds to choosing $n_L = n_3$ and $n_R = n_1$. Hence, we have the following spin states:

$$|\phi_{y_{L}}^{(0)}\rangle = |\phi_{\mathbf{n}_{3}}^{(0)}\rangle = |\downarrow\rangle ,$$

$$|\phi_{y_{L}}^{(1)}\rangle = |\phi_{\mathbf{n}_{3}}^{(1)}\rangle = |\uparrow\rangle ,$$

$$|\phi_{y_{R}}^{(0)}\rangle = |\phi_{\mathbf{n}_{1}}^{(0)}\rangle = |-\rangle := (|\downarrow\rangle - |\uparrow\rangle)/\sqrt{2} ,$$

$$|\phi_{y_{R}}^{(0)}\rangle = |\phi_{\mathbf{n}_{1}}^{(1)}\rangle = |+\rangle := (|\downarrow\rangle + |\uparrow\rangle)/\sqrt{2} .$$
(67)

For the sake of definiteness, we also assume that the magnetic field components vary in the scattering region as follows:

$$\begin{cases}
B_1(y) = B_0 \beta_1(y) \sin^{(2+2q_1)} \left((1+4q_2) \frac{\pi(y-y_L)}{2(y_R-y_L)} \right), \\
B_3(y) = B_0 \beta_2(y) \cos^{(2+2q_1)} \left((1+4q_2) \frac{\pi(y-y_L)}{2(y_R-y_L)} \right), \\
\end{cases} (68)$$

where q_1 and q_2 are again non-negative integer numbers. In this scheme if q_1 increases, both $B_1(y)$ and $B_3(y)$ will nullify in the whole scattering region. Indeed, in the limiting case of $q_1 \to \infty$, with $q_2 = 0$, this scheme reduced to the second example of the model in Appx. G with $n_L = n_3$ and $n_R = n_1$. As for the first scheme, starting from the left lead, the integer q_2 accounts for complete winding of the magnetic field. In order to end with the correct boundary conditions on the right lead, we introduce the two phase function $\beta_1(y)$ and $\beta_2(y)$ (with values ± 1). In the limiting case of $q_2 \to \infty$, we expect to find the same results of the second example of the model described in Appx. G with $n_L = n_3$ and $n_R = n_1$. In this case, the rotation angle is $\alpha = \pi/2$, so that the Berry operator becomes

$$\mathcal{U}_{y_{\mathrm{L}}\to y_{\mathrm{R}}} = \exp\left[-i\left(\frac{\pi}{2}\right)\sigma_{n_{2}}\right] = \frac{1}{\sqrt{2}} \begin{pmatrix} 1 & -1\\ 1 & 1 \end{pmatrix}. \tag{69}$$

We now apply the procedure outlined in Secs. III to compute the transmission matrix t_E . First, we analyze the probability $P_E^{(\downarrow \mapsto -)} = |[t_E]_{0,0}|^2$ which represents the probability for an electron injected in the lowenergy state of the left lead $|\downarrow\rangle$ to be transmitted in the low-energy state of the right lead $|-\rangle$. This, with the corresponding reflection probability $|[r_E]_{0,0}|^2$, are the only scattering processes occurring in the single-channel regime. In the main panel of Fig. 4a), for example, we plot $P_E^{(\downarrow \mapsto -)}$ (green curve) as a function of energy for the case $q_1 = 0$ and $q_2 = 0$. We show that for an injection energy E sufficiently close to E_Z , the electron is fully transmitted, i.e. the probability transmission $P_E^{(\downarrow \mapsto -)}$ reaches 1. On the other hand, for $E \geq E_Z$, we can also define the probability $P_E^{(\uparrow \mapsto -)} = |[t_E]_{0,1}|^2$ (orange curve) for an electron injected in the high-energy state of the left lead $|\uparrow\rangle$ to be transmitted in the low-energy state of the right lead $|-\rangle$, and analogously the transmission

probabilities $P_E^{(\downarrow \mapsto +)} = |[t_E]_{1,0}|^2$ and $P_E^{(\uparrow \mapsto +)} = |[t_E]_{1,1}|^2$ (red curve). As demonstrated in Appendix F, we find that $P_E^{(\uparrow \mapsto -)} = |[t_E]_{0,1}|^2$ is equal to $P_E^{(\downarrow \mapsto +)} = |[t_E]_{1,0}|^2$. The plot shows that $P_E^{(\downarrow \mapsto -)}$ (green curve) monotonically decreases for $E > E_Z$, while $P_E^{(\uparrow \mapsto +)}$ (red curve) rapidly increases, joining the green curve, and thereafter decreasing with it. On the other hand, $P_E^{(\uparrow \mapsto -)}$ monotonically increases from zero for increasing energy. The specific behavior of the various probabilities depends on the details of the scattering region, such as the actual spatial dependence of the Zeeman field B(y) and the length L. This is shown in panels b)-e) of Fig. 4, where the transmission probabilities are plotted for different values of q_1 and q_2 . Panels b) and c) show what happens for increasing q_1 with a fixed value of $q_2 = 0$, namely orange and green curves converge more quickly to 1/2 for $E > E_{\rm Z}$. On the other hand, panels d) and e) presents the behavior of the transmission probabilities for a fixed value of $q_1 = 0$ and $q_2 = 1$ and $q_2 = 10$, respectively. In the latter case all curves collapse on the value 1/2 at $E \geq E_Z$. We emphasize that the asymptotic behavior $(E \gg E_{\rm Z})$ of the curves in Fig. 4 does not depend on the details of B(y) but only on its boundary condition. At odds with respect to Fig. 2, here all probabilities tend to the value 1/2 (denoted by the horizontal black solid line) for large values of energy. This behaviour is actually expected since for $E \gg E_Z$ the transmission matrix reduces to the Berry operator [Eq. (33) in Sec. III]. In the latter, given in Eq. (69), all matrix elements have an absolute squared value equal to 1/2.

As for the Scheme I, we quantify how much the transmission matrix aligns to the Berry operator (69) as a function of the injection energy E, using the Hilbert-Schmidt distances. In the main panel of Fig. 5a) we plot the distance $||t_E(L) - \mathcal{U}_{y_L \to y_R}||_{\text{HS}}$ for $q_1 = 0, 1, 10$, with $q_2 = 0$. In the main panel of Fig. 5b) we plot the Hilbert-Schmidt distance $||t_E^{\text{II}}(L) - \mathcal{U}_{y_L \to y_R}||_{\text{HS}}$ (see the red dashed curve), for the magnetic wall configuration described in Appx. G with $n_L = n_3$ and $n_R = n_1$. Then we quantify the contribution of the back scattering in the process by plotting the distance $||r_E(L)||_{\text{HS}}$ as a function of the injection energy in the inset of Fig. 5a) (the analytical behavior of $||r_E^{\text{II}}(L)||_{\text{HS}}$ is plotted with red dashed line). Similarly, in Fig 5b) we quantify both $||t_E(L) - \mathcal{U}_{y_L \to y_R}||_{\text{HS}}$ (main panel) and $||r_L^{\text{II}}(L)||_{\text{HS}}$ (inset) for $q_2 = 0, 1, 10$, with $q_1 = 0$, as a function of the injection energy E.

We now analyze the scattering process in terms of the incoming and outgoing states, highlighting the role of the Berry operator in the entanglement between the spin degree of freedom and the electron momentum (see, e.g., [21]). Consider an electron injected from the left lead in the low-energy band. For large, but not excessively large energy values (i.e., E moderately larger than $E_{\rm Z}$), the transmission matrix closely approximates the Berry operator described in Eq. (69). Consequently, the outgoing state in the right lead exhibits strong correlations (entanglement) between the spin and kinetic com-

ponents. Specifically, the state can be expressed as

$$|\psi_y^{(E)}\rangle \simeq \frac{e^{ik_E^{(0)}y}|-\rangle + e^{i\gamma}e^{ik_E^{(1)}y}|+\rangle}{\sqrt{2}},\tag{70}$$

where $\gamma := e^{i(k_E^{(1)} - k_E^{(0)})L}$ represents a dynamic phase arising from the free evolution along the scattering region. Similarly, if the incoming state is in the high-energy band, the corresponding outgoing state in the right lead takes the form

$$|\psi_y^{(E)}\rangle \simeq \frac{e^{ik_E^{(0)}y}|-\rangle - e^{i\gamma}e^{ik_E^{(1)}y}|+\rangle}{\sqrt{2}}.$$
 (71)

VII. CONCLUSIONS

In summary, we have proposed a method to describe the coherent transport of electrons through a 1D wire subject to a magnetic field. We have derived a closedform differential equation, which contains both geometric and dynamical contributions, that governs (spinresolved) electron transport for a generic spatially varying magnetic field which interacts with the electrons spin via the Zeeman coupling. We have shown that electrons are fully transmitted when the injection energy is much larger than the Zeeman splitting energy. In this regime, the quantum state of the transmitted electrons undergoes a topological transformation, i.e. the Berry operator of the system. Indeed, such Berry operator depends solely on the values of the magnetic field at the nanowire boundaries, regardless of the magnetic field's behavior within the wire. We have then analyzed two specific examples. In the first one, when the injection energy is below the Zeeman energy, we have demonstrated that perfect spin-flip occurs in the transmission through the wire. In the second example, for injection energies below the Zeeman splitting energy, we observed a balanced spin-mixing. Moreover, for an infinite injection energy (or an infinitesimal wire length), the quantum state of the transmitted electron emerges with a different wavevector in the first example. In the second example, the quantum state becomes entangled between its spin and wavevector degrees of freedom.

We mention that we have checked our results in Figs. 2 and 4 using an independent numerical method which uses a wavefunction matching technique (KWANT toolkit [22]).

To conclude, our approach can be extended to realistic three dimensional nanowires (where multiple transverse modes are present). As long as the number of modes available for transport is restricted to two by choosing the injection energy of electrons within a reduced range of values, we have obtained similar results to the ones reported in Figs. 2 and 4. We mention that a possible implementation of a Zeeman field having the required behavior can be obtained by bending a nanowire in a

uniform magnetic field, or by depositing a nanowire on a substrate containing a magnetic material with a suitable pattern of non-collinear magnetic moments. Examples are Heusler compounds [23], low-dimensional systems which lack structural inversion symmetry, such as a single atomic layer of manganese on a tungsten substrate [24], and other materials, such as insulating multiferroics [25] and van der Waals magnets [26].

ACKNOWLEDGMENTS

F.T. acknowledges funding from MUR-PRIN 2022 -Grant No. 2022B9P8LN - (PE3)-Project NEThEQS "Non-equilibrium coherent thermal effects in quantum systems" in PNRR Mission 4 - Component 2 - Investment 1.1 "Fondo per il Programma Nazionale di Ricerca e Progetti di Rilevante Interesse Nazionale (PRIN)" funded by the European Union - Next Generation EU and the PNRR MUR project PE0000023-NQSTI, and from the Royal Society through the International Exchanges between the UK and Italy (Grants No. IEC R2 192166). V.G. acknowledges financial support by MUR (Ministero dell'Istruzione, dell'Università e della Ricerca) through the following projects: PNRR MUR project PE0000023-NQSTI, PRIN 2017 Taming complexity via Quantum Strategies: a Hybrid Integrated Photonic approach (QU-SHIP) Id. 2017SRN-BRK.

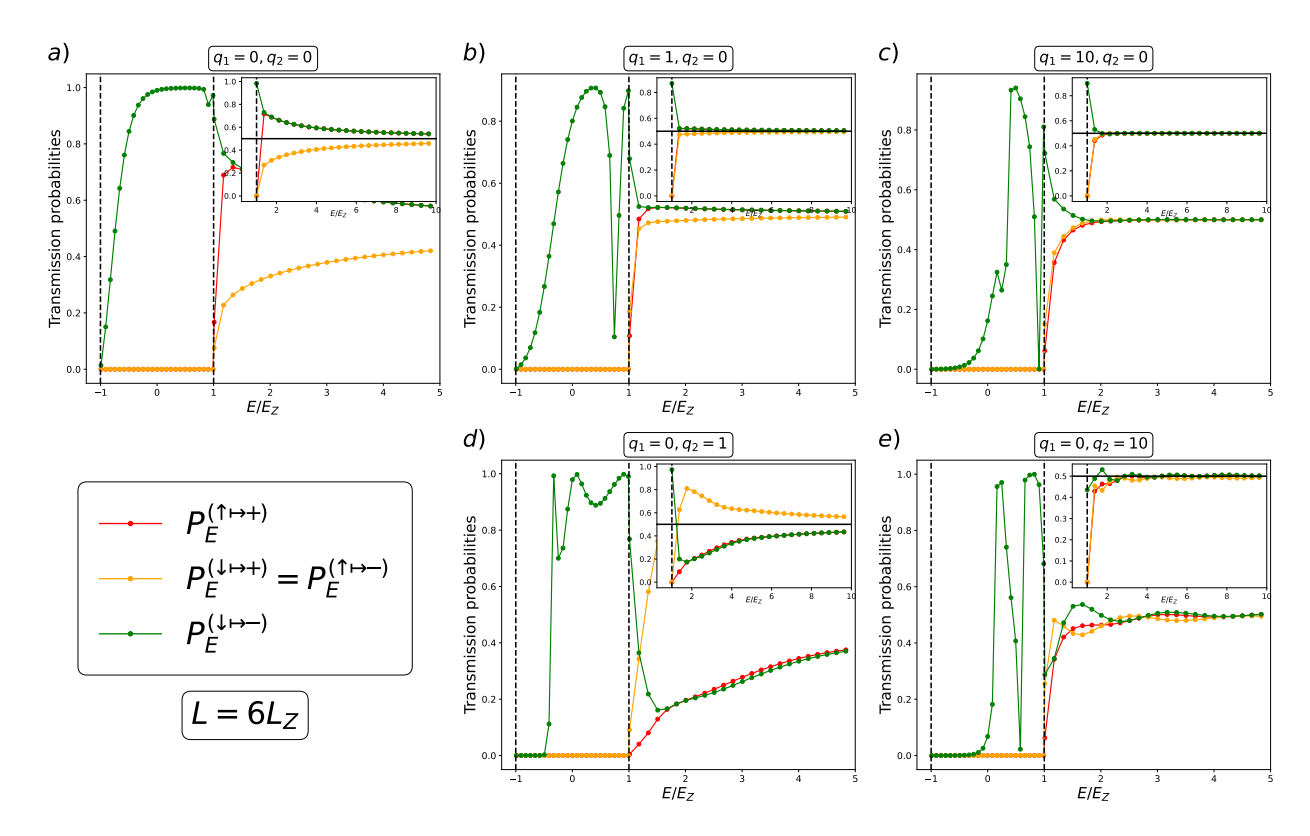


FIG. 4. Transmission probabilities as a function of injection energy for Scheme II (Sec. VIB), with $L=6L_Z$. Each panel corresponds to different values of the parameters q_1 and q_2 , which are specified at the top of each panel. The value of $L=6L_Z$ was selected because it enables nearly perfect spin mixing $(P_E^{\downarrow \mapsto -} \approx 1)$ over the energy range from 0 to E_Z when both parameters are set to zero $(q_1=0, q_2=0)$, as illustrated in panel a). The insets in all plots display an extended energy range, allowing access to the high-energy limit where $E/E_Z \to \infty$. In this limit, for all cases, the red, green and orange curves $(P_E^{\uparrow \mapsto +}, P_E^{\downarrow \mapsto -}$ and $P_E^{\downarrow \mapsto +} = P_E^{\uparrow \mapsto -}$) approach 1/2. This behavior confirms the prediction given by Eq. (C4), where the transmission matrix at large energies coincides with the Berry operator. Notably, this result is independent of q_1 and q_2 , as the Berry operator depends solely on the magnetic field components in the leads [see Eq. (53)].

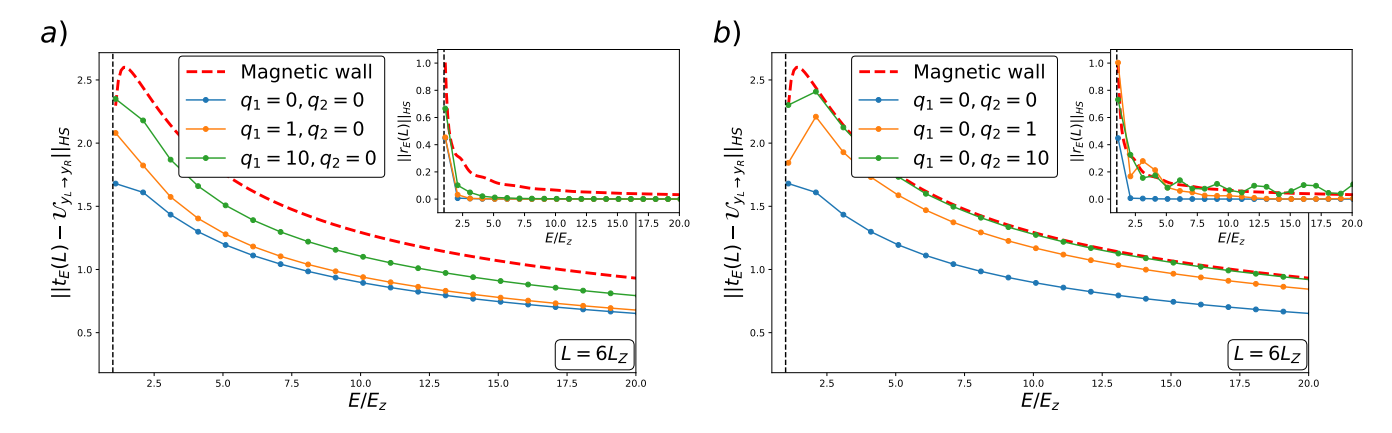


FIG. 5. Scheme II, numerical results for the Hilbert-Schmidt norms $\|t_E(L) - \mathcal{U}_{y_L \to y_R}\|_{\mathrm{HS}}$ and $\|r_E(L)\|_{\mathrm{HS}}$ as a function of injection energy E, plotted as blue, orange, and green dotted curves. The dashed red lines indicate the exact solutions for the distances $\|t_E^{\mathrm{II}}(L) - \mathcal{U}_{y_L \to y_R}\|_{\mathrm{HS}}$ and $\|r_E^{\mathrm{II}}(L)\|_{\mathrm{HS}}$ corresponding to the magnetic wall configuration discussed in Appx. G. In panel a), we vary the integer q_1 ($q_1 = 0, 1, 10$) while keeping $q_2 = 0$ constant. In contrast, in panel b) we fix $q_1 = 0$ and varies q_2 ($q_2 = 0, 1, 10$). In both cases, the distance between the dashed red curve and the dotted curves decreases as either q_1 or q_2 increases. However, the green curve in the inset of panel b) exhibits noticeable jumps, causing it to diverge from the red dashed curve. Although we did not plot the distance $\|r_E(L)\|_{\mathrm{HS}}$ for larger values of q_2 with $q_1 = 0$, we verified that this distance approaches the red dashed curve $\|r_E^{\mathrm{II}}(L)\|_{\mathrm{HS}}$ as $q_2 \to \infty$. This behavior supports our earlier discussion in Appx. G: in the limiting cases where $q_1 \to \infty$ (with $q_2 = 0$) and $q_2 \to \infty$ (with $q_1 = 0$), Scheme II (Sec. VIB) reduces to the magnetic wall configuration with $n_L = n_3$ and $n_R = n_1$.

Appendix A: Current conservation and preliminary observations

In this section we review some basic properties of the model clarifying how the current operator associated with the eigenvector $|\psi_y^{(E)}\rangle$ is expressed in terms of the amplitudes C_y introduced in Eq. (14).

1. Preliminaries

We start by using the transmission and reflection matrices t_E and r_E defined in Eq. (10) to link the coefficients C_{y_L} and C_{y_R} appearing in Eq. (22), in terms of the amplitudes $R_E^{(\ell)}$, $T_E^{(\ell)}$, and $A_E^{(\ell)}$ appearing in Eq. (7).

From Eq. (10) we can write

$$\begin{cases}
T_E^{(\ell)} = \sum_{\ell'=0}^1 \tau_E^{(\ell,\ell')} A_E^{(\ell')} = \sum_{\ell'=0}^1 [t_E]_{\ell,\ell'} \sqrt{\frac{k_E^{(\ell')}}{k_E^{(\ell)}}} A_E^{(\ell')}, \\
R_E^{(\ell)} = \sum_{\ell'=0}^1 \rho_E^{(\ell,\ell')} A_E^{(\ell')} = \sum_{\ell'=0}^1 [r_E]_{\ell,\ell'} \sqrt{\frac{k_E^{(\ell')}}{k_E^{(\ell)}}} A_E^{(\ell')},
\end{cases}$$
(A1)

which, introducing $\boldsymbol{T} := (T_E^{(0)}, T_E^{(1)})^T$, $\boldsymbol{R} := (R_E^{(0)}, R_E^{(1)})^T$, $\boldsymbol{A} := (A_E^{(0)}, A_E^{(1)})^T$, and the matrices

$$W := \begin{pmatrix} 1 & 0 \\ 0 & \sqrt{\frac{k_E^{(1)}}{k_E^{(0)}}} \end{pmatrix} , \qquad W^{-1} := \begin{pmatrix} 1 & 0 \\ 0 & \sqrt{\frac{k_E^{(0)}}{k_E^{(1)}}} \end{pmatrix} , \tag{A2}$$

can be conveniently expressed in the following vectorial form

$$\begin{cases} T = W^{-1}t_E W A, \\ R = W^{-1}r_E W A. \end{cases}$$
 (A3)

Accordingly, setting

$$V := \begin{pmatrix} k_E^{(0)} & 0 \\ 0 & k_E^{(1)} \end{pmatrix} , \qquad F_{L/R} := \begin{pmatrix} e^{ik_E^{(0)}y_{L/R}} & 0 \\ 0 & e^{ik_E^{(1)}y_{L/R}} \end{pmatrix} , \tag{A4}$$

we can rewrite Eq. (27) in the form

$$\begin{bmatrix}
\mathbf{C}_{y_{L}} \\
\mathbf{D}_{y_{L}}
\end{bmatrix} = \begin{bmatrix}
F_{L}\mathbf{A} + F_{L}^{\dagger}\mathbf{R} \\
iV(F_{L}\mathbf{A} - F_{L}^{\dagger}\mathbf{R})
\end{bmatrix} = \begin{bmatrix}
(F_{L} + F_{L}^{\dagger}W^{-1}r_{E}W)\mathbf{A} \\
iV(F_{L} - F_{L}^{\dagger}W^{-1}r_{E}W)\mathbf{A}
\end{bmatrix},$$

$$\begin{bmatrix}
\mathbf{C}_{y_{R}} \\
\mathbf{D}_{y_{R}}
\end{bmatrix} = \begin{bmatrix}
F_{R}\mathbf{T} \\
iVF_{R}\mathbf{T}
\end{bmatrix} = \begin{bmatrix}
F_{R}W^{-1}t_{E}W\mathbf{A} \\
iVF_{R}W^{-1}t_{E}W\mathbf{A}
\end{bmatrix}.$$
(A5)

2. Current conservation

The current operator associated with the spinor eigenstate $|\psi_y^{(E)}\rangle$ is given by

$$\hat{J}_{y}^{(E)} := -\frac{i\hbar}{2m} \left(|\partial_{y} \psi_{y}^{(E)}\rangle \langle \psi_{y}^{(E)}| - |\psi_{y}^{(E)}\rangle \langle \partial_{y} \psi_{y}^{(E)}| \right) , \tag{A6}$$

where for easy of notation we defined $|\partial_y \psi_y^{(E)}\rangle := \partial_y |\psi_y^{(E)}\rangle$. Since $|\psi_y^{(E)}\rangle$ is an eigenvector of $\hat{\mathcal{H}}$ we can write

$$\partial_{y}\hat{J}_{y}^{(E)} = -\frac{i\hbar}{2m} \left(|\partial_{y}^{2}\psi_{y}^{(E)}\rangle\langle\psi_{y}^{(E)}| - |\psi_{y}^{(E)}\rangle\langle\partial_{y}^{2}\psi_{y}^{(E)}| \right)$$

$$= \frac{i}{\hbar} \left[\hat{\mathcal{H}} - \hat{h}_{y}, |\psi_{y}^{(E)}\rangle\langle\psi_{y}^{(E)}| \right]$$

$$= -\frac{i}{\hbar} \left[\hat{h}_{y}, |\psi_{y}^{(E)}\rangle\langle\psi_{y}^{(E)}| \right] , \tag{A7}$$

which represents the continuity equation of the model. Taking the trace of the above identity we arrive to relation $\partial_u \text{Tr}[\hat{J}_y^{(E)}] = 0$ which establishes current conservation along the 1D wire, i.e.

$$\text{Tr}[\hat{J}_y^{(E)}] = -\tfrac{i\hbar}{2m} \left(\langle \psi_y^{(E)} | \partial_y \psi_y^{(E)} \rangle - \langle \partial_y \psi_y^{(E)} | \psi_y^{(E)} \rangle \right) = \text{const }.$$

Expanding the w.r.t. to the decomposition (14) we can rewrite such constraint in the form

$$\sum_{\ell \in \{0,1\}} \left[\left(C_y^{(\ell)} \right)^* D_y^{(\ell)} - C_y^{(\ell)} \left(D_y^{(\ell)} \right)^* \right] + 2 \sum_{\ell,\ell' \in \{0,1\}} \left(C_y^{(\ell)} \right)^* [K_y]_{\ell,\ell'} C_y^{(\ell')} = \text{const.}$$
 (A8)

where we used the fact that the Berry matrix K_y of the process defined in Eq. (17) is skew-symmetric. Expressed in a more compact form we can rewrite the above identity as

$$C_{y}^{\dagger} \cdot D_{y} - D_{y}^{\dagger} \cdot C_{y} + 2C_{y}^{\dagger} \cdot K_{y} \cdot C_{y} = \text{const.}$$
 (A9)

In Appendix B 1 we shall see that this identity corresponds to the symmetry (26) of the matrix $\tilde{\mathcal{M}}^{(E)}$ of Eq. (25). Applying Eq. (A9) at the borders of the scattering region we obtain the identity

$$C_{y_{\mathcal{L}}}^{\dagger} \cdot D_{y_{\mathcal{L}}} - D_{y_{\mathcal{L}}}^{\dagger} \cdot C_{y_{\mathcal{L}}} = C_{y_{\mathcal{R}}}^{\dagger} \cdot D_{y_{\mathcal{R}}} - D_{y_{\mathcal{R}}}^{\dagger} \cdot C_{y_{\mathcal{R}}}, \qquad (A10)$$

where we used the continuity condition (19). Invoking (A5) we can then write

$$\mathbf{C}_{y_{L}}^{\dagger} \cdot \mathbf{D}_{y_{L}} - \mathbf{D}_{y_{L}}^{\dagger} \cdot \mathbf{C}_{y_{L}} = i\mathbf{A}^{\dagger} \left[F_{L}^{\dagger} + W^{\dagger} r_{E}^{\dagger} \left(W^{-1} \right)^{\dagger} F_{L} \right] V \left[F_{L} - F_{L}^{\dagger} W^{-1} r_{E} W \right] \mathbf{A}
+ i\mathbf{A}^{\dagger} \left[F_{L}^{\dagger} - W^{\dagger} r_{E}^{\dagger} \left(W^{-1} \right)^{\dagger} F_{L} \right] V^{\dagger} \left[F_{L} + F_{L}^{\dagger} W^{-1} r_{E} W \right] \mathbf{A}
= i\mathbf{A}^{\dagger} \left[F_{L}^{\dagger} (V + V^{\dagger}) F_{L} - W^{\dagger} r_{E}^{\dagger} \left(W^{-1} \right)^{\dagger} F_{L} (V + V^{\dagger}) F_{L}^{\dagger} W^{-1} r_{E} W \right] \mathbf{A}, \quad (A11)$$

and

$$\boldsymbol{C}_{y_{\mathrm{R}}}^{\dagger} \cdot \boldsymbol{D}_{y_{\mathrm{R}}} - \boldsymbol{D}_{y_{\mathrm{R}}}^{\dagger} \cdot \boldsymbol{C}_{y_{\mathrm{R}}} = i\boldsymbol{A}^{\dagger} \left[W^{\dagger} t_{E}^{\dagger} \left(W^{-1} \right)^{\dagger} F_{\mathrm{R}}^{\dagger} (V + V^{\dagger}) F_{\mathrm{R}} W^{-1} t_{E} W \right] \boldsymbol{A} . \tag{A12}$$

Accordingly Eq. (A10) can be expressed as

$$i\mathbf{A}^{\dagger} \left[F_{L}^{\dagger}(V+V^{\dagger})F_{L} - W^{\dagger}r_{E}^{\dagger} \left(W^{-1}\right)^{\dagger} F_{L}(V+V^{\dagger})F_{L}^{\dagger}W^{-1}r_{E}W - W^{\dagger}t_{E}^{\dagger} \left(W^{-1}\right)^{\dagger} F_{R}^{\dagger}(V+V^{\dagger})F_{R}W^{-1}t_{E}W \right] \mathbf{A} = 0 ,$$
(A13)

which, since it must hold for all choices of the input vector A, can be recast in the operator identity

$$W^{\dagger}r_{E}^{\dagger}\left[\left(W^{-1}\right)^{\dagger}F_{L}(V+V^{\dagger})F_{L}^{\dagger}W^{-1}\right]r_{E}W+W^{\dagger}t_{E}^{\dagger}\left[\left(W^{-1}\right)^{\dagger}F_{R}^{\dagger}(V+V^{\dagger})F_{R}W^{-1}\right]t_{E}W=F_{L}^{\dagger}(V+V^{\dagger})F_{L}. \quad (A14)$$

Consider first the two-channel scenario. Here $k_E(0)$ and $k_E(1)$ are both real so that V and W are Hermitian and $F_{L,R}$ are unitary matrices. Invoking the fact that all commute and using the identity

$$W^{-1}VW^{-1} = k_E^{(0)} \mathbb{1} , (A15)$$

equation (A14) can be expressed as

$$k_E^{(0)}W(r_E^{\dagger}r_E + t_E^{\dagger}t_E)W = V \quad \Longleftrightarrow \quad k_E^{(0)}(r_E^{\dagger}r_E + t_E^{\dagger}t_E) = W^{-1}VW^{-1} = k_E^{(0)}\mathbb{1} , \qquad (A16)$$

that corresponds to (11) in the main text. In the single-channel scenario only $k_E(0)$ is real, while $k_E^{(1)}$ is an imaginary quantity so neither V or W are Hermitian and $F_{L,R}$ are no longer unitary matrices. Since all these operators still commutes it follows that

$$(W^{-1})^{\dagger} F_{L}(V + V^{\dagger}) F_{L}^{\dagger} W^{-1} = (W^{-1})^{\dagger} F_{R}^{\dagger} (V + V^{\dagger}) F_{R} W^{-1} = \begin{pmatrix} 2k_{E}^{(0)} & 0\\ 0 & 0 \end{pmatrix} = 2k_{E}^{(0)} \Pi_{0} ,$$
 (A17)

with $\Pi_0 := \begin{pmatrix} 1 & 0 \\ 0 & 0 \end{pmatrix}$ the projector on the low-energy band of the model. Therefore defining

$$\bar{r}_E := \Pi_0 r_E \Pi_0 = \begin{pmatrix} [r_E]_{00} & 0\\ 0 & 0 \end{pmatrix}, \qquad \bar{t}_E := \Pi_0 t_E \Pi_0 = \begin{pmatrix} [t_E]_{00} & 0\\ 0 & 0 \end{pmatrix},$$
 (A18)

the restrictions of r_E and t_E to the lowest energy level of the model, Eq. (A14) can be written as

$$\bar{r}_E^{\dagger} \bar{r}_E + \bar{t}_E^{\dagger} \bar{t}_E = \Pi_0 \iff |[r_E]_{00}|^2 + |[t_E]_{00}|^2 = 1,$$
 (A19)

as anticipated in the main text. We conclude by reminding that, according to the scattering (Landauer-Büttiker) approach [11], the current flowing in the 1D wire can be expressed in terms of the transmission matrix t_E , via the formula

$$\mathcal{I} = \frac{e}{2\pi\hbar} \int dE \, G_E \left(f_L(E) - f_R(E) \right), \tag{A20}$$

where $f_{L/R}(E)$ are the Fermi function in the left and right leads and $G_E = \text{Tr}\left[t_E^{\dagger}t_E\right]$ in the two-channel scenario, and $G_E = \text{Tr}\left[\bar{t}_E^{\dagger}\bar{t}_E\right] = |[t_E]_{00}|^2$ in the single-channel scenario.

Appendix B: Derivation of the main results

This section is dedicated to show how Eq. (15) leads to Eq. (22), and to discuss how from the latter one can recover the transmission and reflection matrices of the model.

1. Derivation of Eq. (22)

Define the vectors

$$\tilde{C}_y := \mathcal{U}_{y_{\mathcal{I}} \to y}^{\dagger} C_y ,$$
 (B1)

$$\tilde{\boldsymbol{D}}_{y} := \partial_{y} \tilde{\boldsymbol{C}}_{y} = \mathcal{U}_{y_{\mathrm{L}} \to y}^{\dagger} \left(\boldsymbol{D}_{y} + K_{y} \boldsymbol{C}_{y} \right) ,$$
 (B2)

where in the second identity of Eq. (B2) we used

$$\partial_y \mathcal{U}_{y_L \to y} = -K_y \mathcal{U}_{y_L \to y} \Longrightarrow \partial_y \mathcal{U}_{y_L \to y}^{\dagger} = \mathcal{U}_{y_L \to y}^{\dagger} K_y .$$
 (B3)

This allows one to convert Eq. (15) in

$$\partial_y^2 \tilde{\boldsymbol{C}}_y + \frac{2m}{\hbar^2} (E - \tilde{\Omega}_y) \tilde{\boldsymbol{C}}_y = 0 , \qquad (B4)$$

and hence in the first order differential equation

$$\partial_y \begin{bmatrix} \tilde{C}_y \\ \tilde{D}_y \end{bmatrix} = \tilde{\mathcal{M}}_y^{(E)} \begin{bmatrix} \tilde{C}_y \\ \tilde{D}_y \end{bmatrix}, \tag{B5}$$

with $\tilde{\mathcal{M}}_y^{(E)}$ and $\tilde{\Omega}_y$ the matrices defined in Eq. (25). It is worth noticing that the current conservation condition (A9) expressed in terms of \tilde{C}_y and \tilde{D}_y , becomes

$$\tilde{C}_{y}^{\dagger} \cdot \tilde{D}_{y} - \tilde{D}_{y}^{\dagger} \cdot \tilde{C}_{y} = \text{const.}$$
 (B6)

Alternatively we can write this by saying that the first derivative of $\tilde{C}_y^{\dagger} \cdot \tilde{D}_y - \tilde{D}_y^{\dagger} \cdot \tilde{C}_y$ w.r.t. y must be zero, i.e.

$$\partial_y \left(\tilde{C}_y^{\dagger} \cdot \tilde{D}_y - \tilde{D}_y^{\dagger} \cdot \tilde{C}_y \right) = 0 . \tag{B7}$$

Invoking (B5) we can finally notice that, as anticipated in the previous section, (B7) is guaranteed by the symmetry (26) of the matrix $\tilde{\mathcal{M}}^{(E)}$. Indeed we can write

$$\partial_{y} \left(\tilde{C}_{y}^{\dagger} \cdot \tilde{D}_{y} - \tilde{D}_{y}^{\dagger} \cdot \tilde{C}_{y} \right) = \partial_{y} \left(\begin{bmatrix} \tilde{C}_{y}^{\dagger}, \tilde{D}_{y}^{\dagger} \end{bmatrix} \begin{bmatrix} 0 & 1 \\ -1 & 0 \end{bmatrix} \begin{bmatrix} \tilde{C}_{y_{R}} \\ \tilde{D}_{y_{R}} \end{bmatrix} \right)$$

$$= \begin{bmatrix} \tilde{C}_{y}^{\dagger}, \tilde{D}_{y}^{\dagger} \end{bmatrix} \left(\tilde{\mathcal{M}}_{y}^{\dagger(E)} \begin{bmatrix} 0 & 1 \\ -1 & 0 \end{bmatrix} + \begin{bmatrix} 0 & 1 \\ -1 & 0 \end{bmatrix} \tilde{\mathcal{M}}_{y}^{(E)} \right) \begin{bmatrix} \tilde{C}_{y_{R}} \\ \tilde{D}_{y_{R}} \end{bmatrix} = 0.$$
(B8)

The derivation of Eq. (22) of the main text finally follows by integrating the system (B5) over the scattering region, from $y_{\rm L}$ to $y_{\rm R}$. This leads to

$$\begin{bmatrix} \tilde{C}_{y_{R}} \\ \tilde{D}_{y_{R}} \end{bmatrix} = \overleftarrow{\exp} \left\{ \int_{y_{L}}^{y_{R}} dy \tilde{\mathcal{M}}_{y}^{(E)} \right\} \begin{bmatrix} \tilde{C}_{y_{L}} \\ \tilde{D}_{y_{L}} \end{bmatrix} , \tag{B9}$$

which corresponds to Eq. (15) thanks to the identities

$$\tilde{C}_{y_{\mathrm{L}}} = C_{y_{\mathrm{L}}}, \qquad \tilde{C}_{y_{\mathrm{R}}} = \mathcal{U}_{y_{\mathrm{L}} \to y_{\mathrm{R}}}^{\dagger} C_{y_{\mathrm{R}}}, \qquad (B10)$$

$$\tilde{C}_{y_{L}} = C_{y_{L}}, \qquad \tilde{C}_{y_{R}} = \mathcal{U}_{y_{L} \to y_{R}}^{\dagger} C_{y_{R}},
\tilde{D}_{y_{L}} = D_{y_{L}}, \qquad \tilde{D}_{y_{R}} = \mathcal{U}_{y_{L} \to y_{R}}^{\dagger} D_{y_{R}},$$
(B10)

which follows from (B1) and the continuity condition (19).

Transmission and reflection matrices

In this section, we show how to solve the system in Eq. (22) for the matrices r_E and t_E . Before going deeper, we decompose in blocks the ordered exponential in Eq. (22) by writing

$$\tilde{\Gamma}_{y_{\rm L}\to y_{\rm R}}^{(E)} = \overleftarrow{\exp} \left\{ \int_{y_{\rm L}}^{y_{\rm R}} dy \, \tilde{\mathcal{M}}_y^{(E)} \right\} = \begin{bmatrix} X_{0,0} & X_{0,1} \\ X_{1,0} & X_{1,1} \end{bmatrix}, \tag{B12}$$

where each $X_{i,j}$ is a two-by-two matrix. By doing so, Eq. (22) can be equivalently written as

$$\begin{bmatrix} F_{\mathrm{R}}W^{-1}t_{E}W\mathbf{A} \\ iVF_{\mathrm{R}}W^{-1}t_{E}W\mathbf{A} \end{bmatrix} = \begin{bmatrix} \mathcal{U}_{y_{\mathrm{L}}\to y_{\mathrm{R}}} & 0 \\ 0 & \mathcal{U}_{y_{\mathrm{L}}\to y_{\mathrm{R}}} \end{bmatrix} \begin{bmatrix} X_{0,0} & X_{0,1} \\ X_{1,0} & X_{1,1} \end{bmatrix} \begin{bmatrix} (F_{\mathrm{L}} + F_{\mathrm{L}}^{\dagger}W^{-1}r_{E}W)\mathbf{A} \\ iV(F_{\mathrm{L}} - F_{\mathrm{L}}^{\dagger}W^{-1}r_{E}W)\mathbf{A} \end{bmatrix} .$$
(B13)

Exploiting the fact that the above expression must hold for all input vectors \mathbf{A} we can finally translate it into the system (28) which we report here for completeness

$$\begin{cases}
W^{-1}t_{E}W = F_{R}^{\dagger}\mathcal{U}_{y_{L}\to y_{R}}\left(X_{0,0} + iX_{0,1}V\right)F_{L} + F_{R}^{\dagger}\mathcal{U}_{y_{L}\to y_{R}}\left(X_{0,0} - iX_{0,1}V\right)F_{L}^{\dagger}W^{-1}r_{E}W, \\
iVW^{-1}t_{E}W = F_{R}^{\dagger}\mathcal{U}_{y_{L}\to y_{R}}\left(X_{1,0} + iX_{1,1}V\right)F_{L} + F_{R}^{\dagger}\mathcal{U}_{y_{L}\to y_{R}}\left(X_{1,0} - iX_{1,1}V\right)F_{L}^{\dagger}W^{-1}r_{E}W.
\end{cases} (B14)$$

These can be equivalently expressed as

$$\begin{cases}
\left[\mathcal{U}_{y_{L}\to y_{R}}(X_{1,1}V+iX_{1,0})+V\mathcal{U}_{y_{L}\to y_{R}}(X_{0,0}-iX_{0,1}V)\right]W^{-1}r_{E}W = \\
\mathcal{U}_{y_{L}\to y_{R}}(X_{1,1}V-iX_{1,0})-V\mathcal{U}_{y_{L}\to y_{R}}(X_{0,0}+iX_{0,1}V), \\
t_{E}=WF_{R}^{\dagger}\mathcal{U}_{y_{L}\to y_{R}}\left[X_{0,0}+iX_{0,1}V\right]W^{-1}+WF_{R}^{\dagger}\mathcal{U}_{y_{L}\to y_{R}}\left[X_{0,0}-iX_{0,1}V\right]W^{-1}r_{E},
\end{cases} (B15)$$

which we wrote assuming without loss of generality $y_L = 0$, so that $F_L = 1$. By matrix inversion the first equation leads to the following solution for r_E

$$r_{E} = W \left[\mathcal{U}_{y_{L} \to y_{R}}(X_{1,1}V + iX_{1,0}) + V \mathcal{U}_{y_{L} \to y_{R}}(X_{0,0} - iX_{0,1}V) \right]^{-1} \left[\mathcal{U}_{y_{L} \to y_{R}}(X_{1,1}V - iX_{1,0}) - V \mathcal{U}_{y_{L} \to y_{R}}(X_{0,0} + iX_{0,1}V) \right] W^{-1},$$
(B16)

which inserted in the second equation gives t_E . The explicit evolution of this function requires us to to compute (B12), which can be done numerically in the case of interested.

Appendix C: Scattering problem with large injection energy

In this appendix we show how the system in Eq. (22) can be solved analytically in the limiting case (29) obtaining (33). Indeed when the injection energy is much larger than the Zeeman gap, we can invoke the approximation Eq. (30) from which it follows that the matrices W, V, F_R are all proportional to the identity, i.e.

$$W \simeq \mathbb{1}$$
, $V \simeq k_E \mathbb{1}$, $F_R \simeq e^{ik_E y_R} \mathbb{1}$. (C1)

Similarly from Eq. (32) it also follows that

$$X_{0,0} \simeq X_{1,1} \simeq \cos(k_E L) \mathbb{1}$$
, $X_{0,1} \simeq k_E^{-1} \sin(k_E L) \mathbb{1}$, $X_{1,0} \simeq -k_E \sin(k_E L) \mathbb{1}$. (C2)

Accordingly we can conclude that in the limit (29) the following identities hold

$$\mathcal{U}_{y_{\rm L}\to y_{\rm R}}(X_{1,1}V - iX_{1,0}) - V\mathcal{U}_{y_{\rm L}\to y_{\rm R}}(X_{0,0} + iX_{0,1}V) \simeq \mathcal{U}_{y_{\rm L}\to y_{\rm R}}(k_EX_{1,1} - iX_{1,0} - k_EX_{0,0} - ik_E^2X_{0,1})$$

$$= \mathcal{U}_{y_{\rm L}\to y_{\rm R}}(k_E(X_{1,1} - X_{0,0}) - i(X_{1,0} + k_E^2X_{0,1})) = 0 ,$$

$$\mathcal{U}_{y_{L}\to y_{R}}(X_{1,1}V + iX_{1,0}) + V\mathcal{U}_{y_{L}\to y_{R}}(X_{0,0} - iX_{0,1}V) \simeq \mathcal{U}_{y_{L}\to y_{R}}(k_{E}X_{1,1} + iX_{1,0} + k_{E}X_{0,0} - ik_{E}^{2}X_{0,1})
= \mathcal{U}_{y_{L}\to y_{R}}(k_{E}(X_{1,1} + X_{0,0}) + i(X_{1,0} - k_{E}^{2}X_{0,1}))
= 2k_{E}(\cos(k_{E}L) - i\sin(k_{E}L))\mathcal{U}_{y_{L}\to y_{R}}
= 2k_{E}e^{-ik_{E}L}\mathcal{U}_{y_{L}\to y_{R}},$$
(C3)

which replaced into (B15) gives $r_E \simeq 0$ and

$$t_E \simeq W F_{\rm R}^{\dagger} \mathcal{U}_{y_{\rm L} \to y_{\rm R}} \left[X_{0,0} + i X_{0,1} V \right] W^{-1} \simeq e^{-ik_E y_{\rm R}} \mathcal{U}_{y_{\rm L} \to y_{\rm R}} \left(\cos(k_E L) + i \sin(k_E L) \right) = \mathcal{U}_{y_{\rm L} \to y_{\rm R}} ,$$
 (C4)

(recall that Eqs. (B15) assumed $y_L = 0$ so that $y_R = L$, which we used in the last identity to simplify the exponential function).

1. Formal derivation of the quench ansatz

In this section we clarify how the quench ansatz leads to the identity (34). As a prerequisite for this derivation recall that given O a 3×3 real, orthogonal matrix describing a rotation in the 3D cartesian space, its unitary representation $\hat{\mathcal{U}}(O)$ on the Hilbert space induces the following transformation on the Pauli operators

$$\hat{\mathcal{U}}^{\dagger}(O)\hat{\boldsymbol{\sigma}}\hat{\mathcal{U}}(O) = O\hat{\boldsymbol{\sigma}} , \qquad (C5)$$

which, given \boldsymbol{n} a 3D real vector, and $\hat{\boldsymbol{\sigma}}_{\boldsymbol{n}} = \boldsymbol{n} \cdot \hat{\boldsymbol{\sigma}}$ implies

$$\hat{\mathcal{U}}^{\dagger}(O)\hat{\boldsymbol{\sigma}}_{\boldsymbol{n}}\hat{\mathcal{U}}(O) = \hat{\boldsymbol{\sigma}}_{\boldsymbol{n}'}, \qquad \boldsymbol{n}' = O^{-1}\boldsymbol{n},$$
(C6)

Accordingly the eigenvectors $\{|\phi_{n'}^{(\ell)}\rangle\}_{\ell=0,1}$ of $\hat{\sigma}_{n}$ can be related to the eigenvectors $\{|\phi_{n'}^{(\ell)}\rangle\}_{\ell=0,1}$ of $\hat{\sigma}_{n'}$ via the identity

$$\hat{\mathcal{U}}(O) |\phi_{n'}^{(\ell)}\rangle = |\phi_{n}^{(\ell)}\rangle . \tag{C7}$$

a. The quench ansatz

In this large energy regime, one might be tempted to conclude that the scattering process has a negligible impact on the particle's propagation. However, it is important to note that in the present scenario, due to the differing orientations of the magnetic field in the left and right leads, the condition (29) does not necessarily imply that the scattering region can be treated as a minor perturbation. A better ansatz can be obtained by drawing an analogy with dynamical quenches, suggesting that a particle propagating from left to right in the wire "experiences" a sudden, abrupt change in the external magnetic field that leaves the spin invariant and induces no reflections. To better frame this property we find it useful to rewrite the right lead component of the eigenstate $|\psi_y^{(E)}\rangle$ given in Eq. (7) in terms of the local Zeeman spinors of the left lead. This can be done by using Eq. (C7) to write

$$|\phi_{\mathbf{n}_{\mathbf{n}}}^{(\ell)}\rangle = \hat{\mathcal{U}}(O)|\phi_{\mathbf{n}_{\mathbf{n}}}^{(\ell)}\rangle , \qquad \forall \ell \in \{0,1\},$$
 (C8)

with O being a 3×3 real orthogonal matrix which connects n_L and n_R , i.e. $n_R = O n_L$. Observe next that for large E, invoking (30) the solution Eq. (7) can be expressed as

$$|\psi_{y}^{(E)}\rangle \simeq \begin{cases} e^{ik_{E}y} \sum_{\ell \in \{0,1\}} A_{E}^{(\ell)} |\phi_{\mathbf{n}_{L}}^{(\ell)}\rangle + e^{-ik_{E}y} \sum_{\ell \in \{0,1\}} R_{E}^{(\ell)} |\phi_{\mathbf{n}_{L}}^{(\ell)}\rangle , & \forall y \leq y_{L} \\ e^{ik_{E}y} \sum_{\ell \in \{0,1\}} T_{E}^{(\ell)} |\phi_{\mathbf{n}_{R}}^{(\ell)}\rangle = e^{ik_{E}y} \sum_{\ell \in \{0,1\}} T_{E}^{(\ell)} \hat{\mathcal{U}}(O) |\phi_{\mathbf{n}_{L}}^{(\ell)}\rangle , & \forall y \geq y_{R} . \end{cases}$$
(C9)

The quench ansatz requires that for very large E the reflection term disappears, and that the spinor component of the input coincides with the transmitted one, i.e.

$$\begin{split} \sum_{\ell \in \{0,1\}} A_E^{(\ell)} \, |\phi_{\mathbf{n}_{\rm L}}^{(\ell)}\rangle \; &= \; \sum_{\ell \in \{0,1\}} T_E^{(\ell)} \hat{\mathcal{U}}(O) \, |\phi_{\mathbf{n}_{\rm L}}^{(\ell)}\rangle = \sum_{\ell,\ell' \in \{0,1\}} [W^{-1} t_E W]_{\ell,\ell'} A_E^{(\ell')} \hat{\mathcal{U}}(O) \, |\phi_{\mathbf{n}_{\rm L}}^{(\ell)}\rangle \\ &\simeq \; \sum_{\ell,\ell' \in \{0,1\}} [\mathcal{U}_{y_{\rm L} \to y_{\rm R}}]_{\ell,\ell'} A_E^{(\ell')} \hat{\mathcal{U}}(O) \, |\phi_{\mathbf{n}_{\rm L}}^{(\ell)}\rangle \; , \end{split} \tag{C10}$$

where we wrote $T_E^{(\ell)}$ in terms of the input amplitudes $A_E^{(\ell)}$ via the identity (A3) of App. A1 and used Eqs. (33) and (C1). Projecting on $|\phi_{n_L}^{(\ell)}\rangle$ we obtain

$$\sum_{\ell'',\ell'\in\{0,1\}} \langle \phi_{\mathbf{n}_{L}}^{(\ell)} | \hat{\mathcal{U}}(O) | \phi_{\mathbf{n}_{L}}^{(\ell'')} \rangle \left[\mathcal{U}_{y_{L}\to y_{R}} \right]_{\ell'',\ell'} A_{E}^{(\ell')} = A_{E}^{(\ell)} , \qquad (C11)$$

which, since it must hold for all input coefficients $A_E^{(\ell)}$, translates into the following matrix identity,

$$\begin{split} \sum_{\ell'' \in \{0,1\}} \left\langle \phi_{\mathbf{n}_{\mathrm{L}}}^{(\ell)} | \hat{\mathcal{U}}(O) \left| \phi_{\mathbf{n}_{\mathrm{L}}}^{(\ell'')} \right\rangle [\mathcal{U}_{y_{\mathrm{L}} \to y_{\mathrm{R}}}]_{\ell'',\ell'} &= \delta_{\ell,\ell'} & \Longrightarrow & \hat{\mathcal{U}}(O) \sum_{\ell'' \in \{0,1\}} [\mathcal{U}_{y_{\mathrm{L}} \to y_{\mathrm{R}}}]_{\ell'',\ell'} \left| \phi_{\mathbf{n}_{\mathrm{L}}}^{(\ell'')} \right\rangle \left\langle \phi_{\mathbf{n}_{\mathrm{L}}}^{(\ell')} \right| &= \mathbb{1} \\ & \Longrightarrow & \sum_{\ell'' \in \{0,1\}} [\mathcal{U}_{y_{\mathrm{L}} \to y_{\mathrm{R}}}]_{\ell'',\ell'} \left| \phi_{\mathbf{n}_{\mathrm{L}}}^{(\ell'')} \right\rangle \left\langle \phi_{\mathbf{n}_{\mathrm{L}}}^{(\ell')} \right| &= \hat{\mathcal{U}}^{\dagger}(O) \;, \end{split}$$

so that

$$[\mathcal{U}_{\mathbf{y}_{\mathbf{L}}\to\mathbf{y}_{\mathbf{R}}}]_{\ell'',\ell'} = \langle \phi_{\mathbf{n}_{\mathbf{L}}}^{(\ell'')} | \hat{\mathcal{U}}^{\dagger}(O) | \phi_{\mathbf{n}_{\mathbf{L}}}^{(\ell')} \rangle = \langle \phi_{\mathbf{n}_{\mathbf{R}}}^{(\ell'')} | \phi_{\mathbf{n}_{\mathbf{L}}}^{(\ell')} \rangle , \qquad (C12)$$

which corresponds to Eq. (34).

Appendix D: Low-varying field approximation

The derivation of the identities (32) and (35) follow by observing that, for n integer, the block matrix of the form

$$\mathcal{M} = \begin{bmatrix} 0 & \mathbb{1} \\ A & 0 \end{bmatrix} , \tag{D1}$$

fulfils the identities

$$\mathcal{M}^{2n} = \begin{bmatrix} A^n & 0\\ 0 & A^n \end{bmatrix} , \qquad \mathcal{M}^{2n+1} = \begin{bmatrix} 0 & A^n\\ A^{n+1} & 0 \end{bmatrix} . \tag{D2}$$

Accordingly for x real, we can write

$$\exp\left\{x\mathcal{M}\right\} = \sum_{k=0}^{\infty} \frac{x^k \mathcal{M}^k}{k!} = \begin{bmatrix} \sum_{n=0}^{\infty} \frac{x^{2n} A^n}{(2n)!} & \sum_{n=0}^{\infty} \frac{x^{2n+1} A^n}{(2n+1)!} \\ \sum_{n=0}^{\infty} \frac{x^{2n+1} A^{n+1}}{(2n+1)!} & \sum_{n=0}^{\infty} \frac{x^{2n} A^n}{(2n)!} \end{bmatrix} . \tag{D3}$$

In case A is positive semidefinite one has

$$A = \left(\sqrt{A}\right)^2 \,, \tag{D4}$$

so that

$$\sum_{n=0}^{\infty} \frac{x^{2n} A^n}{(2n)!} = \sum_{n=0}^{\infty} \frac{\left(x\sqrt{A}\right)^{2n}}{(2n)!} = \cos\left(x\sqrt{A}\right) , \tag{D5}$$

$$\sum_{n=0}^{\infty} \frac{x^{2n+1} A^n}{(2n+1)!} = \frac{1}{\sqrt{A}} \sum_{n=0}^{\infty} \frac{\left(x\sqrt{A}\right)^{2n+1}}{(2n+1)!} = \frac{1}{\sqrt{A}} \sin\left(x\sqrt{A}\right) , \tag{D6}$$

$$\sum_{n=0}^{\infty} \frac{x^{2n+1} A^{n+1}}{(2n+1)!} = \sqrt{A} \sum_{n=0}^{\infty} \frac{\left(x\sqrt{A}\right)^{2n+1}}{(2n+1)!} = \sqrt{A} \sin\left(x\sqrt{A}\right) , \tag{D7}$$

Accordingly we can write

$$\exp\{x\mathcal{M}\} = \mathcal{D}_x(A) := \begin{bmatrix} \cos\left(x\sqrt{A}\right) & \frac{1}{\sqrt{A}}\sin\left(x\sqrt{A}\right) \\ -\sqrt{A}\sin\left(x\sqrt{A}\right) & \cos\left(x\sqrt{A}\right) \end{bmatrix} . \tag{D8}$$

A similar expression applies also when A is Hermitian but not necessarily positive semidefinite. In such case it is useful to write

$$A = A_+ - A_- \,, \tag{D9}$$

with $A_+, A_- \ge 0$, $A_+A_- = 0$ representing the positive and negative parts of A. Accordingly we have

$$\sqrt{A} = \sqrt{A_{+}} + i\sqrt{A_{-}}, \qquad \frac{1}{A} = \frac{1}{\sqrt{A_{+}}} + \frac{-i}{\sqrt{A_{-}}}, \qquad (D10)$$

and the cosine and sine operators appearing in Eq. (D8) can be computed as

$$\cos\left(x\sqrt{A}\right) = \cos\left(x\sqrt{A_{+}}\right) \oplus \cosh\left(x\sqrt{A_{-}}\right),\tag{D11}$$

$$\sin\!\left(x\sqrt{A_+}\right) \;=\; \sin\!\left(x\sqrt{A_+}\right) \oplus i \sinh\!\left(x\sqrt{A_-}\right) = \sin\!\left(x\sqrt{A_+}\right) + i \sinh\!\left(x\sqrt{A_-}\right) \;, \tag{D12}$$

where the symbol \oplus has been introduced to indicate that the sum must be done by projecting the functions $f(A_{\pm})$ on the support of A_{\pm} . Therefore we can now write

$$\frac{1}{\sqrt{A}}\sin\left(x\sqrt{A}\right) = \frac{1}{\sqrt{A_{+}}}\sin\left(x\sqrt{A_{+}}\right) + \frac{1}{\sqrt{A_{-}}}\sinh\left(x\sqrt{A_{-}}\right),\tag{D13}$$

$$\sqrt{A}\sin(x\sqrt{A}) = \sqrt{A_{+}}\sin(x\sqrt{A_{+}}) - \sqrt{A_{-}}\sinh(x\sqrt{A_{-}}). \tag{D14}$$

Equations (35) and (32) follow finally by setting x = L and taking the operator A in Eq. (D8) equal to Q_E and $-k_E^2\mathbb{1}$ respectively.

1. Infinitesimal scattering regions

In the limit $L \to 0$ from Eq. (35) it follows that

$$\tilde{\Gamma}_{y_{\text{L}} \to y_{\text{R}}}^{(E)} = 1 \implies X_{0,0} = X_{1,1} = 1, X_{1,0} = X_{0,1} = 0.$$
 (D15)

Accordingly the identities (B14) become

$$\begin{cases}
W^{-1}t_E W = \mathcal{U}_{y_L \to y_R} (\mathbb{1} + W^{-1}r_E W), \\
W^{-1}t_E W = V^{-1} \mathcal{U}_{y_L \to y_R} V (\mathbb{1} - W^{-1}r_E W).
\end{cases}$$
(D16)

Introducing the matrix

$$G := \mathcal{U}_{y_{\mathbf{L}} \to y_{\mathbf{R}}}^{\dagger} V^{-1} \mathcal{U}_{y_{\mathbf{L}} \to y_{\mathbf{R}}} V , \qquad (D17)$$

and reorganizing the various terms this leads to the following recursive expression for the reflection matrix

$$(W^{-1}r_EW) = (G - 1) - G(W^{-1}r_EW)$$
(D18)

whose solution can be expressed as

$$(W^{-1}r_EW) = \sum_{k=0}^{\infty} (-G)^k (G-1) = \frac{G-1}{G+1} = \frac{\mathcal{U}_{y_L \to y_R}^{\dagger} V^{-1} \mathcal{U}_{y_L \to y_R} V - 1}{\mathcal{U}_{y_L \to y_R}^{\dagger} V^{-1} \mathcal{U}_{y_L \to y_R} V + 1}$$
(D19)

which can be turned into the second expression of Eq. (39), i.e.

$$r_{E} = \frac{k_{E}^{(0)}(W\mathcal{U}_{y_{L}\to y_{R}}^{\dagger}V^{-1}\mathcal{U}_{y_{L}\to y_{R}}W) - 1}{k_{E}^{(0)}(W\mathcal{U}_{y_{L}\to y_{R}}^{\dagger}V^{-1}\mathcal{U}_{y_{L}\to y_{R}}W) + 1} = \frac{W\mathcal{U}_{y_{L}\to y_{R}}^{\dagger}W^{-2}\mathcal{U}_{y_{L}\to y_{R}}W - 1}{W\mathcal{U}_{y_{L}\to y_{R}}^{\dagger}W^{-2}\mathcal{U}_{y_{L}\to y_{R}}W + 1},$$
 (D20)

with the help of Eq. (A15). Observe that by construction the solution is always self-adjoint, i.e. $r_E^{\dagger} = r_E$. Replacing this into the first of Eq. (B10) we can then arrive at

$$t_{E} = W \mathcal{U}_{y_{L} \to y_{R}}^{\dagger} W^{-1} \frac{2k_{E}^{(0)}(W \mathcal{U}_{y_{L} \to y_{R}} V^{-1} \mathcal{U}_{y_{L} \to y_{R}} W)}{k_{E}^{(0)}(W \mathcal{U}_{y_{L} \to y_{R}}^{\dagger} V^{-1} \mathcal{U}_{y_{L} \to y_{R}} W) + 1}$$

$$= 2k_{E}^{(0)} W V^{-1} \mathcal{U}_{y_{L} \to y_{R}} W \frac{1}{k_{E}^{(0)}(W \mathcal{U}_{y_{L} \to y_{R}}^{\dagger} V^{-1} \mathcal{U}_{y_{L} \to y_{R}} W) + 1}$$

$$= 2W^{-1} \mathcal{U}_{y_{L} \to y_{R}} W \frac{1}{k_{E}^{(0)}(W \mathcal{U}_{y_{L} \to y_{R}}^{\dagger} V^{-1} \mathcal{U}_{y_{L} \to y_{R}} W) + 1}$$

$$= 2W^{-1} \mathcal{U}_{y_{L} \to y_{R}} W \frac{1}{W \mathcal{U}_{y_{L} \to y_{R}}^{\dagger} W^{-2} \mathcal{U}_{y_{L} \to y_{R}} W + 1},$$
(D21)

which corresponds to the first identity of Eq. (39). It is worth observing that the solutions described here could have been directly obtained by imposing continuity conditions of the asymptotic functions (7) at the point $y_{\rm L}$. Notice also

that for $E \to \infty$, $W \to 1$ and Eqs. (D20) and (D21) behave as predicted by Eq. (33).

Appendix E: Scattering problem for piecewise constant elements

As anticipated in the main text, when the magnetic field in the scattering region is piecewise constant, the transfer matrix $\Gamma_{y_L \to y_R}^{(E)}$ can be formally integrated as in Eq. (41). To see this, given $\epsilon > 0$ an infinitesimal increment, we find it useful to introduce two extra points $y_j^{\pm} := y_j \pm \epsilon$ for each of the N+1 elements of the partition (40). Observe that the set of points

$$y_0^- < y_0^+ < y_1^- < y_1^+ < y_2^- < y_2^+ < \dots < y_{N-1}^- < y_{N-1}^+ < y_N^- < y_N^+,$$
 (E1)

identifies a new collection of non overlapping intervals

$$I_j^{(\epsilon)} :=]y_j^-, y_j^+[, I_{j,j+1}^{(\epsilon)} :=]y_j^+, y_{j+1}^-[, (E2)$$

that provide a covering of the scattering region. In particular, $I_j^{(\epsilon)}$ are infinitesimal intervals over which the Berry matrix K_y experience an abrupt change; on the contrary from the properties of (40), it follows that on $I_{j,j+1}^{(\epsilon)}$ the matrix Ω_y assumes constant value Ω_j and the Berry matrix K_y is null, i.e.

$$\begin{cases}
K_{y} = 0, \\
\Omega_{y} = \Omega_{j},
\end{cases}
\qquad \forall y \in I_{j,j+1}^{(\epsilon)} \Longrightarrow \qquad \begin{cases}
\mathcal{U}_{y_{j}^{+} \to y} = \mathbb{1} \\
\tilde{\Omega}_{y} = \Omega_{j}, \\
\mathcal{M}_{y}^{(E)} = \mathcal{M}_{E}^{(j)} := \begin{bmatrix} 0 & \mathbb{1} \\ \frac{2m}{\hbar^{2}} (\Omega_{j} - E\mathbb{1}) & 0 \end{bmatrix} = \begin{bmatrix} 0 & \mathbb{1} \\ -Q_{E}^{(j)} & 0 \end{bmatrix},
\end{cases}$$
(E3)

with $Q_E^{(j)}$ as in Eq. (42). Most importantly each of the intervals (E2) fulfill the continuity condition (19) so that we can invoke the general formula Eq. (22) to propagate the vector $\begin{bmatrix} C_y \\ D_y \end{bmatrix}$ across them. Specifically, for all j we can write

$$\begin{bmatrix} \boldsymbol{C}_{y_j^+} \\ \boldsymbol{D}_{y_j^+} \end{bmatrix} = \Gamma_{y_j^- \to y_j^+}^{(E)} \begin{bmatrix} \boldsymbol{C}_{y_j^-} \\ \boldsymbol{D}_{y_j^-} \end{bmatrix} , \qquad \begin{bmatrix} \boldsymbol{C}_{y_{j+1}^-} \\ \boldsymbol{D}_{y_{j+1}^-} \end{bmatrix} = \Gamma_{y_j^+ \to y_{j+1}^-}^{(E)} \begin{bmatrix} \boldsymbol{C}_{y_j^+} \\ \boldsymbol{D}_{y_j^+} \end{bmatrix} , \tag{E4}$$

which by concatenation gives

$$\Gamma_{y_{\rm L}^- \to y_{\rm R}^+}^{(E)} = \Gamma_{y_0^- \to y_N^+}^{(E)} = \Gamma_{y_0^- \to y_N^+}^{(E)} \Gamma_{y_{N-1}^+ \to y_N^-}^{(E)} \cdots \Gamma_{y_1^+ \to y_2^-}^{(E)} \Gamma_{y_1^- \to y_1^+}^{(E)} \Gamma_{y_0^+ \to y_1^-}^{(E)} \Gamma_{y_0^- \to y_0^+}^{(E)}. \tag{E5}$$

The identity (41) follows from this by invoking (38) to compute the transfer matrix over the infinitesimal intervals $I_i^{(\epsilon)}$, i.e.

$$\Gamma_{y_j^- \to y_j^+}^{(E)} = \begin{bmatrix} \mathcal{U}_j & 0\\ 0 & \mathcal{U}_j \end{bmatrix}, \qquad \mathcal{U}_j := \mathcal{U}_{y_j^- \to y_j^+}, \tag{E6}$$

and using Eq. (E3) to write

$$\Gamma_{y_j^+ \to y_{j+1}^-}^{(E)} = \exp\left\{ \int_{y_j^+}^{y_{j+1}^-} dy \mathcal{M}_E^{(j)} \right\} = \exp\left\{ (y_{j+1}^- - y_j^+) \mathcal{M}_E^{(j)} \right\} = \mathcal{D}_{L_j}(Q_E^{(j)}) , \qquad (E7)$$

where we used the identity (D8) with $A = Q_E^{(j)}$ and $x = y_{j+1}^- - y_j^+ = L_j$.

Appendix F: Property of the scattering matrix

The transmission and reflection matrices t_E and r_E computed for electrons injected from the left lead, contribute in defining the scattering matrix S_E via the identity,

$$S_E = \begin{bmatrix} r_E & t_E' \\ t_E & r_E' \end{bmatrix} , \tag{F1}$$

with t'_E (r'_E) being the transmission (reflection) matrix for electrons injected from the right lead. As discussed in Ref. [27], for a given position-dependent magnetic field $\mathbf{B}(y)$, the matrix S_E satisfies the reciprocity relation

$$S_E(\boldsymbol{B}(y)) = [S_E(-\boldsymbol{B}(y))]^T, \tag{F2}$$

where the superscript T means transpose. From Eq. (F2) and (F1) follow straightforwardly that

$$t_E(\mathbf{B}(y)) = [t'_E(-\mathbf{B}(y))]^T, \qquad r_E(\mathbf{B}(y)) = [r'_E(-\mathbf{B}(y))]^T.$$
 (F3)

Now we will show that, under two specific conditions, the scattering problem for electrons that are injected from the left lead with B(y) is formally equivalent to the scattering problem for electrons that are injected from the right lead with the reverse field, -B(y). More precisely, if these two conditions are satisfied, the system in Eq. (22) is identical for the two scattering problems, meaning that

$$t_E(\mathbf{B}(y)) = t_E'(-\mathbf{B}(y)). \tag{F4}$$

The first condition is that $[\Omega_y]_{\mathbf{B}(y)} = [\Omega_{y'}]_{\pm \mathbf{B}(y')}$ where $y \in [y_L, y_R]$ and $y' =: y_L + y_R - y$ so that $y' \in [y_R, y_L]$. In other words, the Zeeman eigenvalues, contained in the matrix Ω_y , must be symmetric with respect to the middle point of the scattering region. The second condition is that $\mathcal{U}_{y_L \to y}|_{\mathbf{B}(y)} = \mathcal{U}_{y_R \to y'}|_{-\mathbf{B}(y')}$, which holds true if $\theta_y|_{\mathbf{B}(y)} = \theta_{y'}|_{-\mathbf{B}(y')}$, see Eq. (53). Combining Eq. (F3) with Eq. (F4), it is straightforward to find

$$t_E(\mathbf{B}(y)) = [t_E(\mathbf{B}(y))]^T \implies [t_E]_{0,1} = [t_E]_{1,0}.$$
 (F5)

Notice that in the Example II (Sec.VIB) both conditions are satisfied, leading to the property in Eq. (F5). On the other hand, in the Example I (Sec.VIA), the first condition is satisfied, while the second one is not. Indeed, we find $|\theta_y|_{B(y)} = |\theta_{y'}|_{B(y')}$, meaning that $|\mathcal{U}_{y_L \to y}|_{B(y)} = |\mathcal{U}_{y_R \to y'}|_{B(y')}$. Although we are not able to prove it, numerically in this case we find $|[t_E]_{0,1}|^2 = |[t_E]_{1,0}|^2$.

Appendix G: Magnetic wall

In this section, we define an analytically solvable scattering problem, and we refer to this configuration as a "magnetic wall". The leads are subjected to two magnetic fields of equal magnitude, B_0 , pointing in different directions, $n_{\rm L}$ and $n_{\rm R}$:

$$\boldsymbol{B}_{L} = B_0 \boldsymbol{n}_{L}, \quad \boldsymbol{B}_{R} = B_0 \boldsymbol{n}_{R}. \tag{G1}$$

In the scattering region (length L), the magnetic field is zero. This configuration represents a limiting case of Scheme I (Sec. VI A) and Scheme II (Sec. VI B). In both schemes, the magnetic wall configuration is achieved when $q_1 \to \infty$ with $q_2 = 0$, or when $q_2 \to \infty$ with $q_1 = 0$. Specifically, Scheme I reduces to a magnetic wall with $\mathbf{n}_L = \mathbf{n}_3$ and $\mathbf{n}_R = -\mathbf{n}_3$, while Scheme II reduces to a magnetic wall with $\mathbf{n}_L = \mathbf{n}_3$ and $\mathbf{n}_R = \mathbf{n}_1$. Analytical solutions exist for the reflection and transmission matrices, $r_E^{\mathrm{I/II}}(L)$ and $t_E^{\mathrm{I/II}}(L)$, of the magnetic wall configuration in Schemes I and II. These solutions (valid for any magnetic field direction in the leads) are found by matching the spinor wavefunction and its first y-derivative at $y = y_L$ and $y = y_R$. Due to space constraints, we do not provide the analytical forms for Scheme I. Instead, we present the Hilbert-Schmidt norms $\|t_E^{\mathrm{I}}(L) - \mathcal{U}_{y_L \to y_R}\|_{\mathrm{HS}}$ in Fig. 3 (red dashed curve, main plots) and $\|r_E^{\mathrm{I}}(L)\|_{\mathrm{HS}}$ (red dashed curve, inset plots). Analogously, Fig. 5 displays the distances $\|t_E^{\mathrm{II}}(L) - \mathcal{U}_{y_L \to y_R}\|_{\mathrm{HS}}$ (red dashed curve, main plots) and $\|r_E^{\mathrm{II}}(L)\|_{\mathrm{HS}}$ (red dashed curve, inset plots) for Scheme II.

- [1] P. Harvey-Collard et al., Phys. Rev. X 12, 021026 (2022)
- [2] A.M.J. Zwerver et al., PRX Quantum 4, 030303 (2023)
- [3] H.B. van Ommen et al., PRX Quantum 6, 020309 (2025)
- [4] M. Büttiker, Phys. Rev. B 46, 12485 (1992)
- [5] Y. Imry and Rolf Landauer, Rev. Mod. Phys. 71, S306 (1999)
- [6] D. A. Bagrets and Yu. V. Nazarov, Phys. Rev. B 67, 085316 (2003)
- [7] T. Ando, Rev. Mod. Phys. **54**, 437 (1982)
- [8] H. F. Cheung, E. K. Riedel, and Y. Gefen Phys. Rev. Lett. 62, 587 (1989)
- [9] C. W. J. Beenakker, Rev. Mod. Phys. **69**, 731 (1997)
- [10] S. Cusumano et al., Phys. Rev. Lett. 124, 190401 (2020)
- [11] Y. M. Blanter and M. Büttiker, Phys. Rep., 336, 1 (2000)
- [12] The Berry Operator was firstly introduced in Ref [20].
- [13] M. Popp, D. Frustaglia and K. Richter, Phys. Rev. B 68, 041303(R) (2003)

- [14] M. Hentschel et al., Phys. Rev. B **69**, 155326 (2004)
- [15] E. J. Rodríguez and D. Frustaglia Phys. Rev. B 104, 195308 (2021)
- [16] S. A. Wolf et al., Science **294**, 1488 (2001)
- [17] S. Das Sarma, American Science, 89, 516 (2001)
- [18] A. Hirohata, Journal of Magnetism and Magnetic Materials, 509, 166711 (2001)
- [19] I. Žutić, J. Fabian, and S. Das Sarma, Rev. Mod. Phys. 76, 323 (2004)
- [20] F. Wilczek and A. Zee, Phys. Rev. Lett. **52**, 2111 (1984)
- [21] S. Souma and B. K. Nikolić, Phys. Rev. B 70, 195346 (2004)
- [22] C. W. Groth et al., New J. Phys. 16, 063065 (2014)
- [23] K. Manna et al., Nat. Rev. Mater. 3, 244 (2018)
- [24] M. Bode et al., Nature **447**, 190 (2007)
- [25] D. Khomskii, Physics 2, 20 (2009)
- [26] K. Du et al., Adv. Mater. **35**, 2303750 (2023)
- [27] S. Datta and B. Das, Appl. Phys. Lett. **56**, 665 (1990)